Microfluidic Tools to Investigate Protein Crystallization

A Dissertation

Presented to

The Faculty of the Graduate School of Arts and Sciences

Brandeis University

Biophysics and Structural Biology Program

Seth Fraden (Physics Department), Advisor

In Partial Fulfillment

of the Requirements for the Degree

Doctor of Philosophy

by

Michael Heymann

February, 2014

This dissertation, directed and approved by Michael Heymann's committee, has been accepted and approved by the Graduate Faculty of Brandeis University in partial fulfillment of the requirements for the degree of:

DOCTOR OF PHILOSOPHY

Malcolm Watson, Dean of Arts and Sciences

Dissertation Committee:

Seth Fraden (Physics Department), Chair

Daniel Pomeranz Krummel (Biochemistry Department)

Jeff Gelles (Biochemistry Department)

Abstract

Microfluidic Tools to Investigate Protein Crystallization

A dissertation presented to the Faculty of
the Graduate School of Arts and Sciences of
Brandeis University, Waltham, Massachusetts

by Michael Heymann

There is no guarantee that a given protein has a crystalline phase, but even existence of an equilibrium crystalline phase is not sufficient for a crystal to form because the transformation of a protein solution to a crystal is governed by two non-equilibrium processes: nucleation and growth. Consequently, supersaturation kinetics play an essential role in crystallization and we argue that the optimal crystallization strategy should screen kinetic trajectories involving variables such as depth of supersaturation, duration of supersaturation, and sample volume. We have developed a Phase Chip technology based on emulsion microfluidics in which nanoliter volumes of protein solution are encapsulated in oil and stabilized by surfactant. Crystallization is a stochastic process; we experimentally optimize crystal nucleation and growth by generating hundreds of different kinetic paths simultaneously by varying both temperature and concentration of the protein solution. By using a dialysis membrane, one can optimize kinetic trajectories against various small molecule solutes, like salts, pH and surfactants. We also made the Phase Chip compatible with *in situ* diffraction studies by synchrotron diffraction. This entails finding conditions on-chip for which one crystal is grown per drop and then isolating hundreds of drops stored on a x-ray transparent microfluidic device. Single, non-cryoprotected crystals were too small and sensitive to radiation damage to collect a complete diffraction data set of isomorphous crystals at room temperature, but a full data set could be obtained by merging many single diffraction patterns.

Contents

List of Tables

List of Figures

Chapter 1

Introduction

1.1 Protein crystal nucleation and growth

Understanding protein function through protein structure is fundamental for biological sciences. Protein crystallography remains the primary method for protein structure determination by x-ray diffraction. Growing crystals of sufficient size and quality continues to pose a major challenge despite tremendous progress in robotic automation and recent advances in microfluidic technology to screen crystallization conditions. The transformation of a protein solution to a crystal is governed by two non-equilibrium processes: nucleation and growth.

While the precise physical nature of crystal nucleation remains poorly understood [1, 2, 3], classical nucleation theory predicts that crystal nucleation is favored at high levels of supersaturation (Figure 1.1). In classic nucleation theory a crystal is a sphere with radius r and thus the free energy (ΔG) of a crystal nucleus is considered to be:

$$\Delta G = \left(4\Pi r^2\right)\gamma - \left(\frac{4}{3}\Pi r^3\right)\Delta\mu, \tag{1.1}$$

with γ as the surface tension cost contributed from the crystal surface, and $\Delta\mu$ as the

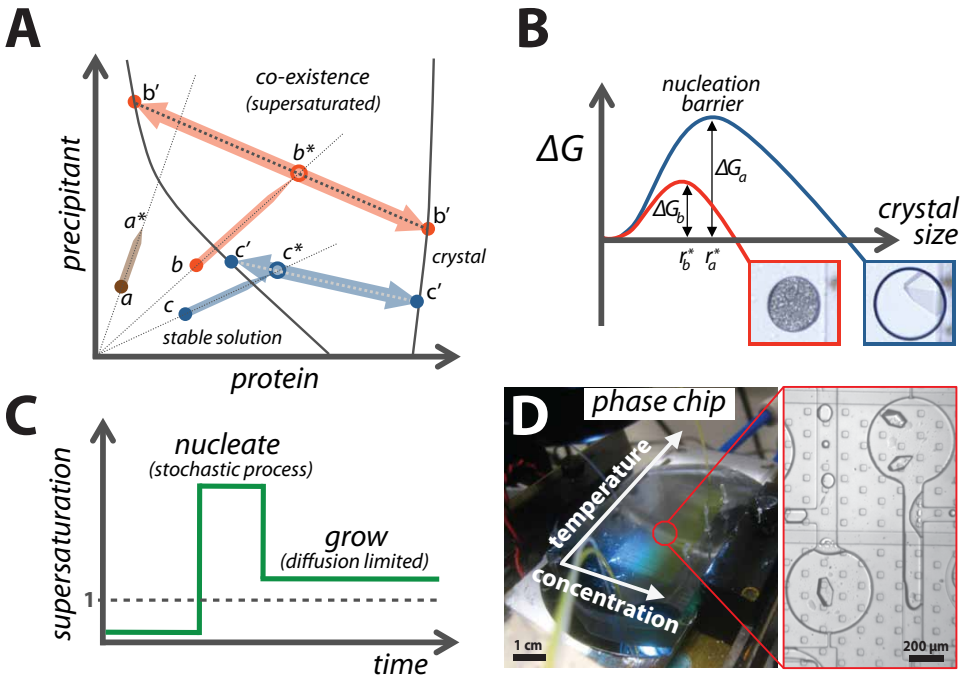

Figure 1.1: (A) Classic crystallization trials like vapor diffusion follow a limited trajectory in phase space. Crystallization cocktails with composition a, b and c would not yield diffraction quality crystals. After the two-fold concentration increase during vapor diffusion the resulting a^* would still be below the solubility limit, b^* would be to deeply supersaturated and yield showers of small crystals, and c^* would be too mildly supersaturated, such that the associated nucleation barrier renders nucleation so unlikely that the protein already denatures before a critical nucleus could form. (B) Hypothetical nucleation barriers for kinetic pathways in (A). The nucleation barrier ΔG_b is to low, yielding showers of crystals. The barrier ΔG_a is to high, rendering nucleation unlikely. (C) Ideally a kinetic pathway should thus nucleate one crystal at high supersaturation that can then grow at low supersaturation. (D) For this we developed the Phase Chip to be able to reversibly program supersaturation and screen for and ideal kinetic pathway, by adjusting temperature and concentration in various combinations in parallel.

chemical potential difference between crystal phase and liquid phase. I other words, an energy cost associated from creating new surface in solution is countered by a free energy gain from transferring material out of solution into the crystal phase. As both energies scale differently with radius, a critical nucleus size can be considered to be:

$$r^* = \frac{2\mu}{\rho\Delta\mu} \tag{1.2}$$

leading to free energy barrier of nucleation

$$\Delta G^* = kT \left(\frac{16\Pi}{3kT} \cdot \frac{\gamma^3}{\rho^2 \Delta\mu^2} \right). \tag{1.3}$$

Hence the nucleation rates is

$$\Gamma \sim e^{\frac{-\Delta G^*}{kT}}, \tag{1.4}$$

and fast for low barrier heights ΔG^*, which are lowest for low surface tensions γ and a high free chemical potential differences $\Delta\mu$. Typically, the surface tension γ of a nucleus can only be lowered to some degree. Polymers like polyethylene glycol have been reported to act as 'surfactants' interacting with the nucleus surface and thus lowering the nucleation barrier [4]. The chemical potential difference $\Delta\mu$ strongly depends the depth of supersaturation, which scales directly with concentration or protein and salt [5, 6]. In conclusion, high supersaturation favors crystal nucleation.

Crystal growth in turn is primarily diffusion limited and a high supersaturation translates into a fast growth rates, while commonly slow growth rates are preferred to minimize defect formation during growth (Figure 1.1 C) [1].

1.2 Protein crystallization in microfluidic systems

To tackle the challenge of protein crystallization, various labs have thought to exploit the precise control over solution condition in space and time inherent to microfluidic technology, as was recently reviewed [7, 8].

In one approach pioneered in the Quake lab, a poly-dimethylsiloxane (PDMS) chip containing several thousand pneumatic control wells were actuated to fill nanoliter sized sample chambers with protein and precipitant to control their mixing by free interface diffusion [10, 11], or a combination of free interface diffusion and vapor

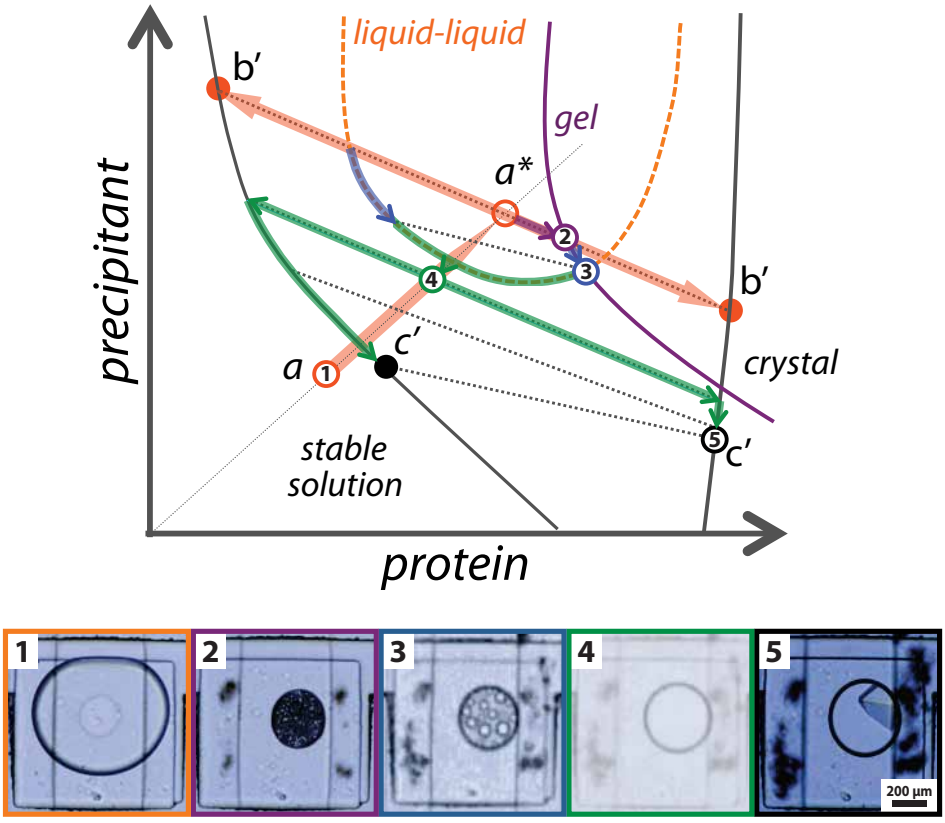

Figure 1.2: Optimized kinetic path for crystallization. An initial drop of Lysozyme and Peg is formulated to be below the solubility limit at point a (frame 1). The droplet then shrinks as water evaporates until it becomes highly supersaturated (point a^*). In classic vapor diffusion the droplet would phase separate towards b' (frame 2), but fail to nucleate a crystal as protein would gel out of solution at the gel-boundary. With the Phase Chip the supersaturation can be reduced again by swelling the droplet, allowing the transition into the liquid-liquid co-exsistance zone (frame 3). Further swelling up the droplet by water influx results again in a clear drop (frame 4). However, due to the journey into the highly supersaturated regime a crystal nuclei has formed that now can grow into a large crystal at c'(frame 5). A quench directly to the low supersaturation at 4 failed to crystallize due to the high nucleation barrier at this level of supersaturation. Experimental data from [9].

diffusion [12, 13]. Due to the valve architecture the cost per experiment were very high and a complex external pressure control system was required to operate the chip. The technology was commercialized in 2003 by Fluidigm, but eventually they discontinued their crystallography product line in 2012.

In another approach pioneered in the Ismagilov lab, microbatch-style crystallization trials were encapsulated into nanoliter sized droplets and spaced by an immiscible carrier fluid [14, 15, 16]. The dropmaker was designed such that drop composition and size could be varied to explore the crystallization phase diagram. This plug-based technology including a work station to set-up chips was commercialized by Emerald Biosystems [17, 18]. More recently, the Ismagilov lab developed a user-loaded SlipChip for equipment-free mircobatch and free-interface diffusion crystallization [19]. This device was easy to operate and comparably cheap to manufacture.

While the plug-based crystallization system was investigated in combination with crystal seeding [20], all these microfluidic approaches to protein crystallization neglected that crystal nucleation and crystal growth require opposing degrees of supersaturation [1]. To decouple nucleation and growth, the Phase Chip has been developed [9, 21]. With the Phase Chip, the kinetic pathway of crystallization can be optimized (Figure 1.2). In another approach, the Kenis lab combined microfluidic control with classic vapor diffusion to achieve reversiblity of crystallization trajectories [22].

1.3 Chapter Overview

This dissertation details advances in fabricating microfluidic devices. In Chapter 2 we present process improvements to fabricate multi-hight photoresist masters with large aspect ratios through selective development of alignment marks. In Chapter 3 we introduce a chemical masking method to pattern microfluidic surface properties, which we exploit in formulating double emulsions.

Also, we have developed new microfluidic tools for protein crystallization. Chapter 4 details a microfluidic platform to kinetically screen crystallization conditions in high throughput through dialysis. A new microfluidic approach to high-throughput

serial crystallography with synchrotron radiation is covered in Chapter 5.

Finally, in Chapter 6 we investigate the Belousov-Zhabotinzky (BZ) reaction as a substrate for computation using soft-lithography to fabricate logic gates from heterogeneous substrates.

Chapter 2

Multi-height precision alignment with selectively developed alignment marks

Michael Heymann, Seth Fraden, and Dongshin Kim

(This chapter was accepted for publication in the Journal of Microelectromechanical Systems (JMEMS) on August 5th 2013. Reproduced with permission from IEEE/ASME.)

Abstract

The alignment step in fabricating multi-height photoresist masters is a critical and time-consuming process. SU8 masters that combine very thin and thick layers can be difficult to align, due to low contrast visibility. We increase visual contrast by selectively developed alignment marks to ease fabrication of masters with thick resist layers deposited on much thinner ones. In addition, we use a vernier calliper based

alignment mark to achieve high precision alignment.

2.1 Introduction

Multi-height designs are both common and critical to a wide range of microfluidic applications, e.g. the chaotic herringbone mixer [23], surface tension guided drop storage [21], sub micrometer drop fabrication [24], *E.coli* trap device (mother machine) [25], elastomer stamping [26], electronically programmable membranes [27], and to pattern hydrophobicity on surfaces by using nanometer deep micro-patterns [19]. Fabricating multi-level masters is challenging and time consuming. Typically, after depositing, exposing and baking the first photoresist layer, a second level of photoresist is spun and soft baked onto the master. The photomask for the second layer is then aligned with the master using dedicated alignment marks exposed into the first resist layer (Figure 2.1, middle panel). Due to this sequential build-up of photoresist, the first layer alignment marks are always immersed by uncured photoresist of the second layer and therefore, their optical contrast is reduced. If the second layer is thicker than the first layer, the alignment marks may become too faint to be resolved in standard reflection microscopy. This approach also limits the number of additional layers to be built onto the master, since the second level mark becomes exposed into the resist.

To overcome these optical limitations, different techniques have been used. Mata et al.[29] dry etched their alignment marks directly into the silicon wafer to build masters with up to six photoresist layers. Alternatively, positive photoresist marks can be deployed onto a wafer in a first preparative step [28] (Figure 2.1, right panel). Because of their amber-red color, marks from positive resist (AZ or SPR) are easily seen through subsequently deposited negative resist layers. Both methods have the

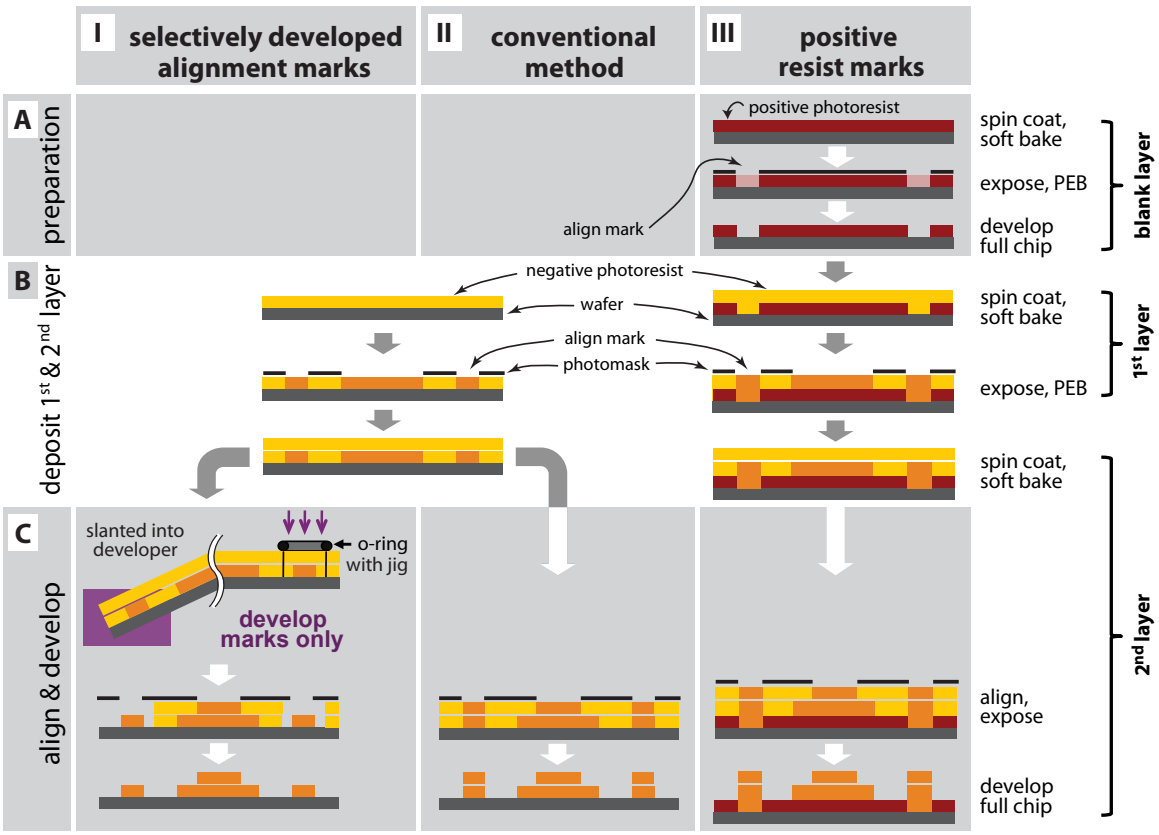

Figure 2.1: Schematic comparison of methods to fabricate multi-height masters. Our method to selectively develop alignment marks (left column) and the conventional method (middle column) share a common first step (B I&II): After the 1st layer photoresist was spun and exposed to UV-light, the 2nd layer photoresist was spun. (C I) After soft baking the 2nd layer photoresist, the align marks were selectively developed as illustrated in Figures 2.3 to 2.5. Subsequent procedures including alignment, exposure and development were the same for all three methods. The center column (II) shows the conventional microfabrication method without selective development of alignment marks. The right column (III) shows how positive photoresist can be used to distinguish the alignment mark by its amber-red color [28].

advantage that building the marks is independent from building the features and the heights of both can be chosen independently. However, silicon dry etching is a complex technique and not accessible to many microfluidics labs that mostly build PDMS devices outside of a traditional clean room. Furthermore, if one is constructing a multi-height photoresist master composed solely of negative resist, then both the dry etch and positive resist alignment methods require an independent manufacturing step. In each case it is desirable to save the labor time and material cost by building the alignment marks along with the features. Another disadvantage of both the dry etch and positive photoresist approaches is that the wafer has already been processed and the surface has to be cleaned again before depositing the first negative resist layer. Inevitably one ends up with a poorer surface than the original polished wafer, especially if a blank foundation layer of positive resist is used [28].

In this paper, we introduce a new method for photo-mask alignment to make multi-height negative SU8 photoresist masters in which the alignment marks have high optical contrast and do not require additional spin coats of resist. We increase alignment mark visibility by developing the non-exposed (non-cross linked) photo resist in the region around the alignment mark. In the crudest implementation, we tilted the master in a bath of developer such that only the edge of the master with the alignment mark is submerged. Alternatively, we use a spin-coater to develop the mark in order to minimize the developed area. In a more sophisticated version, we constructed a jig to isolate the portion of the wafer containing the alignment mark for development. Our approach does not require extra resources or equipment and can be implemented easily in other labs. Another advantage is that no photoresist from the second layer remains over the first layer alignment marks so that the second layer alignment marks are not constructed on top of the first layer marks. Therefore, one can deposit multiple layers of features without obscuring the original mark.

2.2 Results and experimental procedures

2.2.1 Vernier caliper alignment mark

We demonstrate the selective development of alignment marks method using a simple vernier scale alignment mark [30, 31], as shown in Figure 2.2. We match the size of our mark to fit into the field of view of our contact aligner (ABM Mask Aligner, ABM Inc.) equipped with a Zeiss MJM Split Field Microscope at 50 x final magnification. With a 1 mm large mark we can achieve an alignment precision of 2.5 μm in both principal directions. If desired, even sub-micron precision can be achieved by rescaling the vernier.

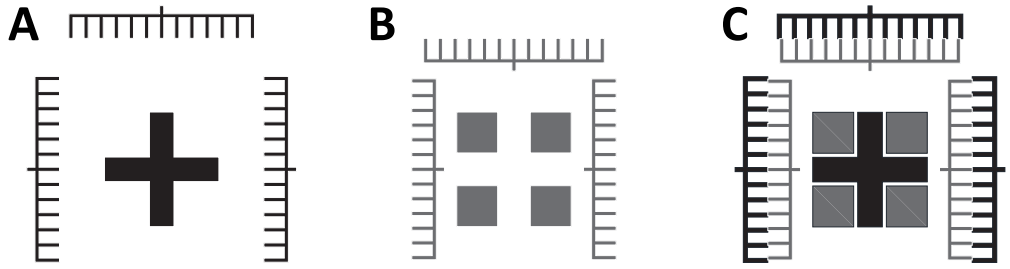

Figure 2.2: Vernier caliper alignment mark for the first layer (A) mask, and second layer (B) mask. (C) View when mask (B) is aligned over the developed photoresist (A). Graduations are 90 μm wide and the squares (in B and C) have an edge length of 250 μm. The alignment precision of this vernier scale is 2.5 μm.

2.2.2 Three methods for selective alignment mark developement

We manufactured several masters with alignment marks exposed into a 5 μm thick SU8-2005 layer. We then spin coated a second layer of SU8-2000 series negative resist of varying thickness. SU8 resists were purchased from MicroChem Inc. and processed as described by the product information. After the second level resist soft bake had been completed, we selectively developed the alignment marks using one of three different techniques:

(1) The master was carefully dipped sideways into a bath with developer so that the mark was immersed in developer solution, but the device features remained undeveloped (Figure 2.3). To prevent developer contacting the unexposed resist in the region about to be exposed to UV-light, the developer was only agitated very gently. Developing the alignment mark on a 100 μm thick SU8 master took about 10 minutes.

(2) Using a Hamilton gas tight syringe we deposit a few microliters of developer solution over the mark. After a 2 min incubation, we remove the softened resist by spinning the wafer at 500 rpm for 5 seconds with acceleration of 100 rpm/second and subsequently 3000 rpm for 30 seconds with acceleration of 300 rpm/second on the spin-coater (Figure 2.4). We repeat these develop-and-spin cycles until the mark is sufficiently cleared for further processing. Usually, two rounds suffice to remove a 100 μm resist layer to achieve good mark visibility for alignment. We then bake the wafer for 2 min at 65 ℃ and 2 min at 95 ℃ to evaporate away remaining developer.

(3) Alternatively, we use a dedicated clamp to further speed up the development process while also reducing the area developed around the mark (Figure 2.5). It was important to clean spilled resist from the backside of the master with a cloth soaked in developer and then dry with a stream of nitrogen gas. We placed the

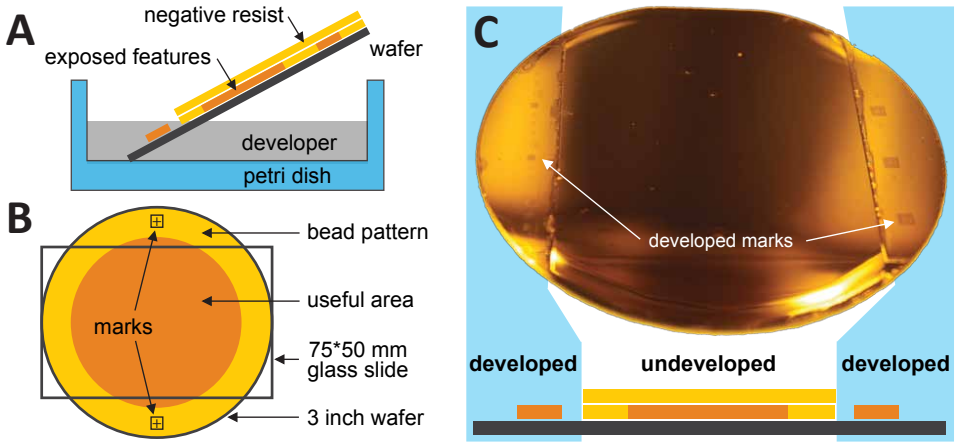

Figure 2.3: Slanted wafer for selectively developed alignment mark method. (A) A wafer was dipped sideways into a bath of developer to selectively develop a 1 cm wide sector containing the marks. (B) Thick SU8 films form a pronounced edge bead, causing varying resist thickness within approximately 1 cm of the rim (yellow). While microfluidic channels are preferably not placed into this rim, it is well suited for alignment marks. Furthermore, most microfluidic devices adopt a rectangular footprint, so that essentially no ′useful′ wafer space (orange) is consumed by the slanted wafer method. Top view (C) of an alignment mark test pattern on a 3-inch wafer after selective development, including a schematic cross section below. Developed areas are highlighted in blue.

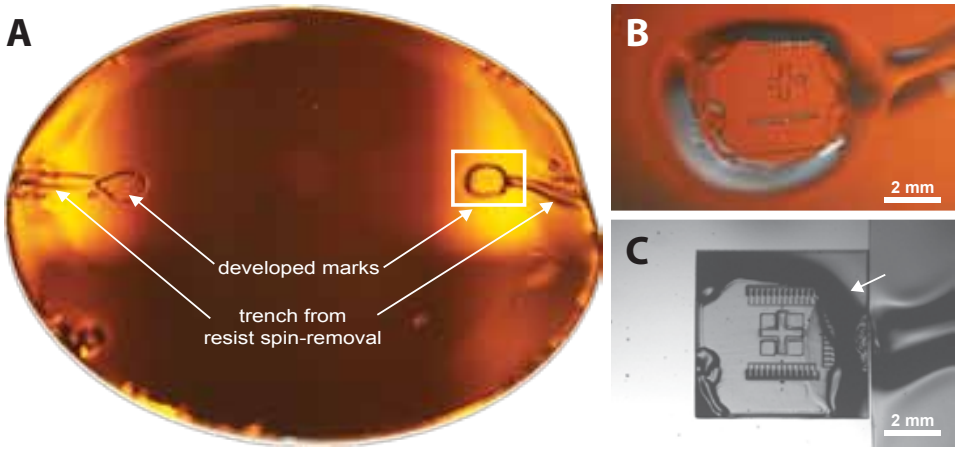

Figure 2.4: Selective alignment mark development with spin-removal of developed resist. (A) 3 μm of developer was placed onto each alignment mark and allowed to soften the resist for 2 minutes. The resist was the removed using a spin-coater. (B) Mark after two cycles of development with spin-removal, prior to UV-light exposure. (C) Stereomicroscope image of final wafer after complete development and hard bake. The transition zone from developed area to unaffected resist (arrow) is about 1 mm thick.

master on a glass plate and mounted it into a jig, where O-rings limited the developer solution to be in contact only with the region around the alignment mark. We then used a plastic Pasteur pipette to flush the mark with developer and isopropanol by repeatedly aspirating and re-injecting the respective solutions. We found this process to be quite effective, as even a 100 μm thick SU8 layer was fully developed after 30 seconds. Residual isopropanol in the access well was dried away using a stream of nitrogen gas.

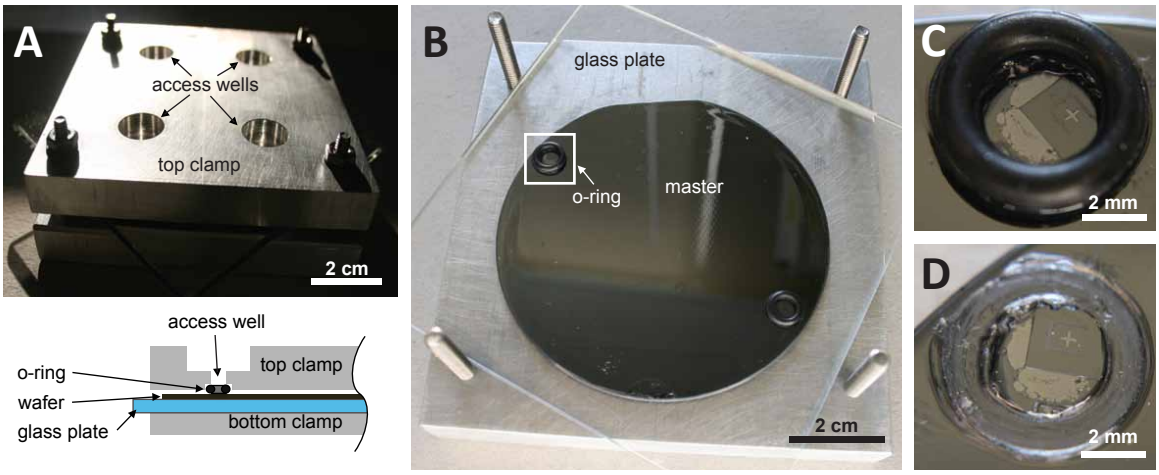

Figure 2.5: Clamp to selectively develop alignment marks. (A) An aluminum clamp was machined with 4 access wells. The back of the master is cleaned to ensure an even and flat surface. (B) The master is then centered on a glass plate and the lid with the O-rings is carefully lowered onto the master and fixed in position by gently fastening the screw nuts manually. After the alignment marks were developed the clamp was disassembled. The white square (B) highlights the alignment mark before (C) and after (D) the O-rings were removed.

2.2.3 Mark visibility comparison for different resist thicknesses

Using bright field reflection microscopy we compared the visibility of our masters (Figure 2.6). Because the optics of our contact aligner split field microscope could not resolve 5 μm thick marks covered with more than 25 μm SU8, we used an Olympus BX51 with an AVT Marlin firewire camera to image our masters. The illumination conditions were kept constant and only the focus was adjusted slightly to maximise contrast. We measured intensity profiles along the vernier using ImageJ [32]. The optical contrast deteriorated strongly with increasing thickness once the second resist layer was thicker than 10 μm (Figure 2.6). Only for the case of a thin second resist layer was the alignment mark visibility improved in comparison to the post exposure baked first resist layer. We attribute this to the fact that the low viscosity SU8 photo resist formulations, tailored for coating up to 10 μm thin films, contained enough solvent to dissolve the upper portions of the first resist layer, which was partially removed during spin coating of the second layer resulting in improved optical contrast. In all cases the visibility of the alignment marks was dramatically improved upon developing the alignment marks. We did not notice a significant difference in alignment mark visibility between the three techniques and all three methods can remove the uncured resist completely.

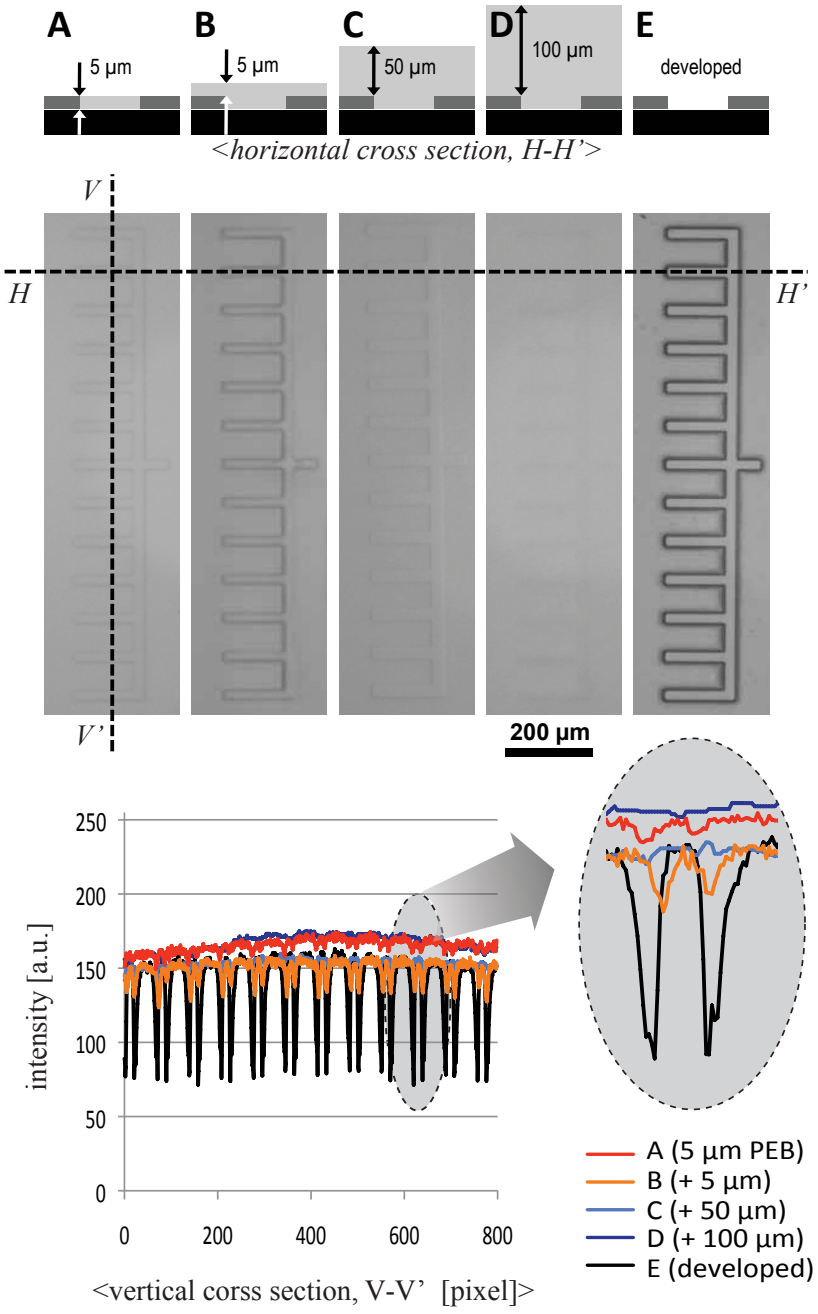

Figure 2.6: Alignment mark visibility for 5 μm thick SU8-2005 after (A) post-exposure bake and after (E) partial development. For comparison a 5 μm thick SU8-2005 photoresist layer with a second layer of SU8-2000 series of thickness (B) 5 μm, (C) 50 μm, and (D) 100 μm after pre-exposure bake. The vertical line over the alignment vernier (V-V′ in A), indicate where the intensity profiles were scanned.

2.3 Conclusion

We found each of the three techniques to selectively develop alignment marks to be robust and reliable, however specific applications might favor one over the other. The transition from selectively developed portion to unaffected resist was smaller than 2 mm in all cases. The developer only affected the exposed region and we did not observe the developer to cut through or go under the photo resist.

While technically the easiest approach, the slanted wafer technique (Figure 2.3) needs the most time to develop a given mark. Both marks have to be developed sequentially, but one can easily batch process wafers this way. The space consumed for this method roughly matches the smallest hemi-circle to contain the mark, plus a few millimeters safety margin (Figure 3B). Thick SU8 films form a pronounced edge bead and accordingly microfluidic channels are usually not placed within the approximately 1 cm wide rim zone of the wafer that is most affected by the edge bead. We place our alignment marks into this peripheral zone, because the edge bead does not affect alignment accuracy. Furthermore, most microfluidic devices adopt a rectangular footprint. For instance, a design tailored for a standard 2 x 3 inch microscope slide, leaves an excess half-inch segment on each half of the 3 inch wafer. Each of these segments is large enough for selective development. As a result, no $'$useful$'$ wafer space is consumed.

The spin-removal technique (Figure 2.4) consumes significantly less space on the wafer and also is faster than the slanted wafer technique, but requires more attention when applying the developer to the mark. For second resist layers thicker than 50 μm this technique requires multiple iterations. We get best results with depositing 3 μm to develop a mark with about 2 mm edge length. This method is sensitive to the amount of developer deposited, as too big a puddle will easily spread out beyond the

target area. When spinning the softened resist away, a trench remains, which limits this approach to marks placed on the perimeter of a design only.

The clamp-assisted method (Figure 2.5) is the most controlled way to apply developer to defined regions. While this technique takes the most time to set-up, actual development proceeds the fastest, rendering this approach ideal for very thick resist layers of about 150 μm and thicker. The space consumed in this method exactly matches the outer diameter of the O-rings used. This clamp-assisted method is also useful in case one desires to use selective development with already old/previously designed photomasks that have the alignment marks in the middle of the design. If one can reuse photomasks, it will reduce the process cost which is especially a concern with expensive chrome photomasks.

Selectively developing the alignment marks makes the fabrication of multilevel masters simpler and more robust than current master preparation methods and facilitates the fabrication of large and complex chip designs with multiple resist layers. We showed three different techniques to selectively develop the marks and highlighted their respective advantages and disadvantages.

Independent of the specific optics available, our method allows the alignment of masks when the height of the second layer of resist is greater than the first layer with a minimum of extra processing steps. This ability will greatly benefit the microfluidics community in light of the many new rigid materials for making microfluidic devices that help to overcome the stringent height-to-width aspect ratio limitations of traditional PDMS features, which rarely exceed ratios of 1:10 height to width, e.g. microfluidic stickers (see Sollier et al.[33] for a review), sol-gel chips [34] , and embossed plastics [35], which have recently been pioneered. The resolutions used in most microfluidic applications do not require clean rooms. Because it is less expensive and more convenient, the soft-lithography community is increasingly working outside of

the clean room. The selective development of alignment marks method is intended for this community. This method is also intended for those facilities that do not possess dry-etchers, such as in smaller universities and in developing countries. To selectively develop alignment marks eases the fabrication of multi-height, high-aspect ratio devices.

Acknowledgements

This work was supported by the NSF MRSEC (DMR-0820492) and the Pioneer Research Center Program through the National Research Foundation of Korea (2013-005772).

Chapter 3

Functional patterning of PDMS microfluidic devices using integrated chemo-masks

Mark B. Romanowsky, Michael Heymann, Adam R. Abate, Amber T. Krummel, Seth Fraden, and David A. Weitz

(This chapter was originally published in Lab on a Chip [36] and was slightly edited for this dissertation. Reproduced with permission from the Royal Society of Chemistry.)

Abstract

Microfluidic devices can be molded easily from PDMS using soft lithography. However, the softness of the resulting microchannels makes it difficult to photolithographically pattern their surface properties, as is needed for applications such as double emulsification. We introduce a new patterning method for PDMS devices, using integrated oxygen reservoirs fabricated simultaneously with the microfluidic chan-

nels, which serve as chemo-masks. Oxygen diffuses through the PDMS to the nearby channel segments and there inhibits functional polymer growth; by placement of the chemo-masks, we thus control the polymerization pattern. This patterning method is simple, scalable, and compatible with a variety of surface chemistries.

3.1 Introduction

The material of choice for many kinds of microfluidic devices is PDMS. Using soft lithography, it can be molded quickly, easily, and at low cost [37]. Additional advantages of PDMS include its gas permeability, which makes it useful in cell patterning or culturing applications [38], and its low elastic modulus, which makes it useful for devices incorporating valves [39, 40]. Increasingly complex, integrated arrays of devices and components have been demonstrated [41, 42]. However, some microfluidic applications require spatially patterned surface properties; for example, double emulsions (drops within drops) can generally be made only in channels whose wettability switches abruptly between hydrophilic and hydrophobic [43, 44]. This kind of functional patterning remains challenging for PDMS devices, despite the many surface modification methods now available [45]. Individual double emulsion makers have been patterned via photo-polymerization, by passing light through a photo-mask [46, 47] or by a finely focused beam of light [48], but both these methods require precise alignment of the mask or beam to the microfluidic channels. This alignment is a major hurdle for larger devices or device arrays, due to the softness of PDMS. To functionally pattern a cm-scale array at μm-scale precision, the photo-mask must be aligned with the microchannels to 1 part in 10^4, but PDMS is so soft that even small stresses can distort it beyond this tolerance. Moreover, PDMS is known to shrink during curing: devices are smaller than their soft lithography masters by 1-2%

in linear size, and the amount of shrinkage depends on the details of the elastomer base-crosslinker mix and the curing conditions [49]. Therefore a photo-mask must be tailored not only to a specific device design but also a highly specific fabrication protocol. To address these difficulties, an improved functional patterning method for PDMS is needed.

In this paper, we introduce a new method for patterned surface functionalization of PDMS microfluidic channels using integrated "chemo-masks", which exploits the gas permeability of PDMS. The chemo-masks are oxygen reservoirs near but not connected to the fluid channels, molded in the elastomer during the same soft lithography process. Oxygen diffuses out of the reservoirs and inhibits polymerization in the nearby channel segments, thereby imposing a chosen polymer growth pattern. The chemo-masks and flow channels are molded simultaneously, so the alignment step and specialized optics needed by photo-mask techniques are avoided. The chemo-masks automatically scale identically with the channels, so elastomer strain and shrinkage become unimportant. The chemo-masks function independently of the particular chemistry initiating the polymerization, so non-photo-initiators can be used instead of photo-initiators, allowing us to pattern polymer growth even without a UV light source. We show that the chemo-mask method works robustly in a range of device geometries, and show its utility by using it to make devices to produce double emulsions of both water-oil-water and oil-water-oil types.

3.2 Results and experimental procedures

3.2.1 The chemo-mask method

We demonstrate the chemo-mask method using simple microfluidic devices, consisting of one flow channel plus one set of chemo-masks, shown in Figure 3.1a. A straight

channel of width 30 μm is abutted, along a segment of length L, by two rectangular chambers separated from the channel by a thin wall of thickness 20 μm. The rectangular chambers have a width of 1500 μm, which together with their length controls the amount of atmospheric oxygen they contain. All features are 50 μm high. We make the devices from PDMS using standard soft lithography methods [39]. We remove the PDMS from the master, punch inlet and outlet holes for the channels, and plasma bond to a glass slide. The PDMS and glass slide are removed from the plasma source before being brought together, so air is trapped in the chemo-mask chambers.

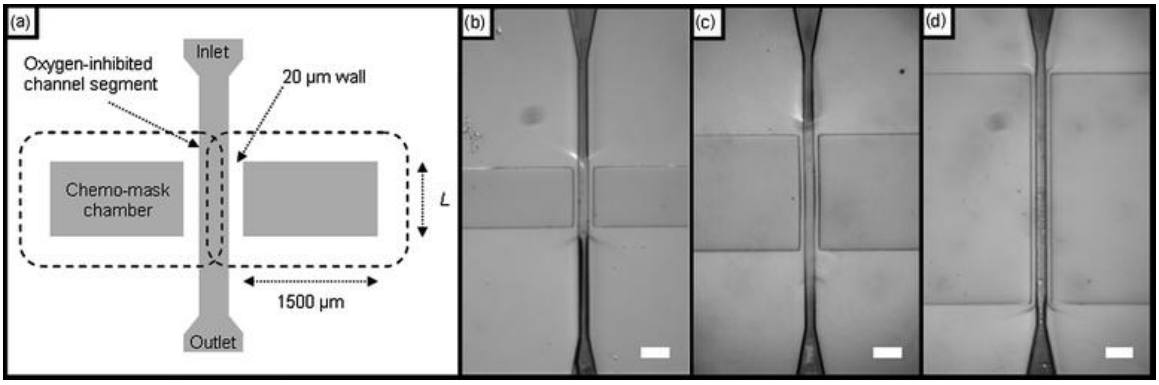

Figure 3.1: Device schematic (a, not to scale), and micrographs of patterned devices stained for visualization (b, c, and d). Oxygen diffuses readily from the chemo-mask chamber, through a short interval of PDMS, and into the nearby channel segment, inhibiting polymerization there. Chemo-mask length L is varied to control the channel segment in which polymerization is inhibited: L is 200, 400, and 800 μm in panels b, c, and d. The height of all features is 50 μm. Scale bars denote 100 μm.

We functionalize the channels with two further steps. First, we apply a glassy coating using a sol-gel method [48]. This coating is a polycondensed silane network with two kinds of functional groups: fluorocarbon groups, which make the coating hydrophobic by default; and photo-initator groups, which will provide surface-bound radicals to initiate polymer growth. Second, we fill the fluid channel with an acrylic acid monomer solution [48] and expose the whole device to UV light at intensity 140 mW cm^2 for 10 minutes; this is done in air, without degassing. Poly(acrylic

acid) (PAA) grows on all the channel surfaces, and makes them hydrophilic, except for regions close to the chemo-masks. Oxygen, trapped in the chemo-mask chambers during bonding, diffuses through the thin walls into the neighboring channel segments and inhibits the polymerization. A similar inhibition effect has been exploited to make complex polymer particles [50, 51] and to shape photo-curable adhesives using PDMS molds [52]. We can suppress the inhibition if desired, allowing polymerization everywhere, by pre-filling the chemo-mask chambers with water. After UV exposure, we flush the channel with water to remove unbound monomer.

To visualize the pattern of polymerization, we stain the channel with toluidine blue dye. This stain binds electrostatically only to the surfaces with PAA, darkening the whole channel except for the regions near the chemo-mask where polymerization was inhibited, as shown in Figure 3.1 b-d. The dye is dissolved at 0.1% (w/w) in pH 8 phosphate buffer solution. We apply the stain for 5 minutes, then flush with water, and purge with air.

3.2.2 Chemo-mask design parameters

The length of the inhibited region in the channel corresponds to the length of the chemo-mask chamber, and this length is the most useful design parameter. The wall thickness of 20 μm is an empirical tradeoff between structural stability and permeability: 10 μm walls do not reliably survive fabrication, and 40 μm walls do not reliably pass enough oxygen to fully inhibit polymerization. Micrographs of devices with 20 μm and 40 μm walls, with visualized polymerization patterns, are shown in Figure 3.2 a-b; the device in the bottom left panel is identical to the one shown in Figure 3.1. In the device with 20 μm walls, we see a clear masking effect; in the device with 40 μm walls, a masking effect can be still seen, but it is not as pronounced.

Other characteristics of the chemo-mask have less influence on the shape of the

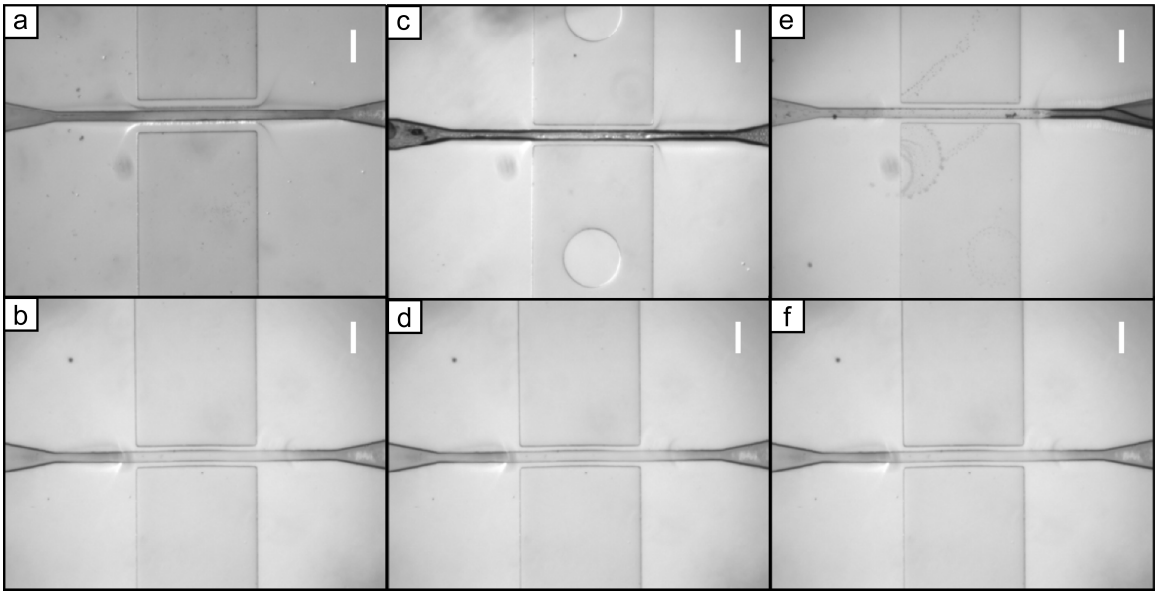

Figure 3.2: Micrographs of stained chemo-mask devices, with walls 40 μm thick (b) or 20 μm thick (a), with reservoirs 750 μm wide (c) or 1500 μm wide (d), and with height of all features 15 μm (e) or 50 μm (f). Scale bars denote 100 μm.

inhibited region. The area of the chemo-mask reservoirs (length times width for these rectangular reservoirs) must be great enough to hold sufficient oxygen to fully inhibit polymerization by counteracting all available initiator molecules. We find that width of 750 μm is a threshold at which there is just enough oxygen in the reservoir to provide masking; chemo-masks with greater width and more oxygen still cover roughly the same channel region (Figure 3.2 c-d). We see negligible change in the inhibited region when varying the feature height from 10 to 50 μm. Devices with height 50 μm and 15 μm have similar inhibited regions, as shown in the micrographs of Figure 3.2 e-f.

Chemo-masks may be used to pattern flow channels up to 100 μm wide (Figure 3.3); wider channels may be incompletely inhibited, especially near the corners of the chemo-mask chambers. The length of the inhibited region is similar for 20 μm, 30 μm, and 100 μm wide channels, although it has slightly irregular ends in the 100 μm wide channel. We note that the chemo-mask reservoirs for these devices are

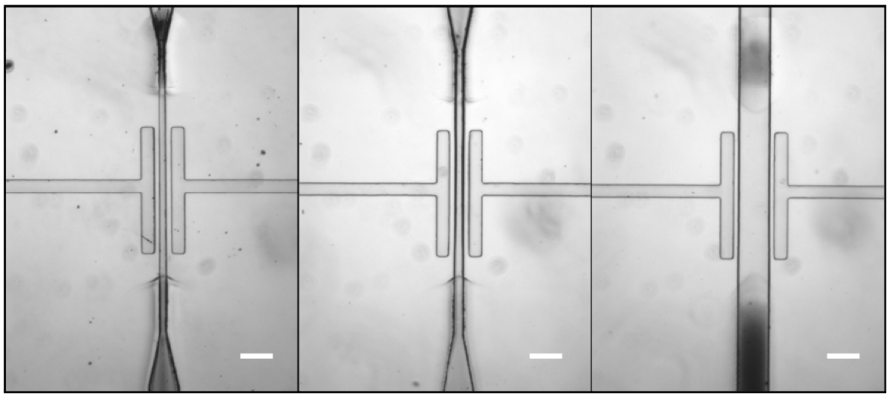

Figure 3.3: Micrographs of stained chemo-mask devices, with flow channels of width 20 μm (left), 30 μm (center), or 100 μm (right). Scale bars denote 100 μm.

an irregular shape, but they have similar total area to the rectangular chemo-masks above.

3.2.3 Chemo-masks for double emulsion dropmaker

To demonstrate the usefulness of the chemo-mask patterning method, we use it to make devices for producing double emulsions. This is a stringent test of the method, because double emulsions can be formed only in devices with a strong and sharp change in wettability. We use the same patterning protocol as above, except that we reduce UV exposure to 1 minute, which generates enough wetting contrast to make double emulsions. To make water-oil- water double emulsion, we use a device with two consecutive cross junctions. Our chemo-mask is placed near the first junction and the subsequent channel, to keep these regions hydrophobic, while the second junction and the rest of the device becomes hydrophilic. A schematic of the junctions and chemo-mask is shown in Figure 3.4 a, and a corresponding micrograph of the device producing double emulsions is shown in Figure 3.4 b. We use a similar device to make oil-water-oil double emulsions; its chemo-mask covers the second junction and the outlet channel to keep them hydrophobic, while the rest of the device becomes hydrophilic. A schematic and micrograph of the oil-water-oil device are shown in Figure 3.4c and Figure 3.4d, respectively. Both devices stably produce monodisperse double

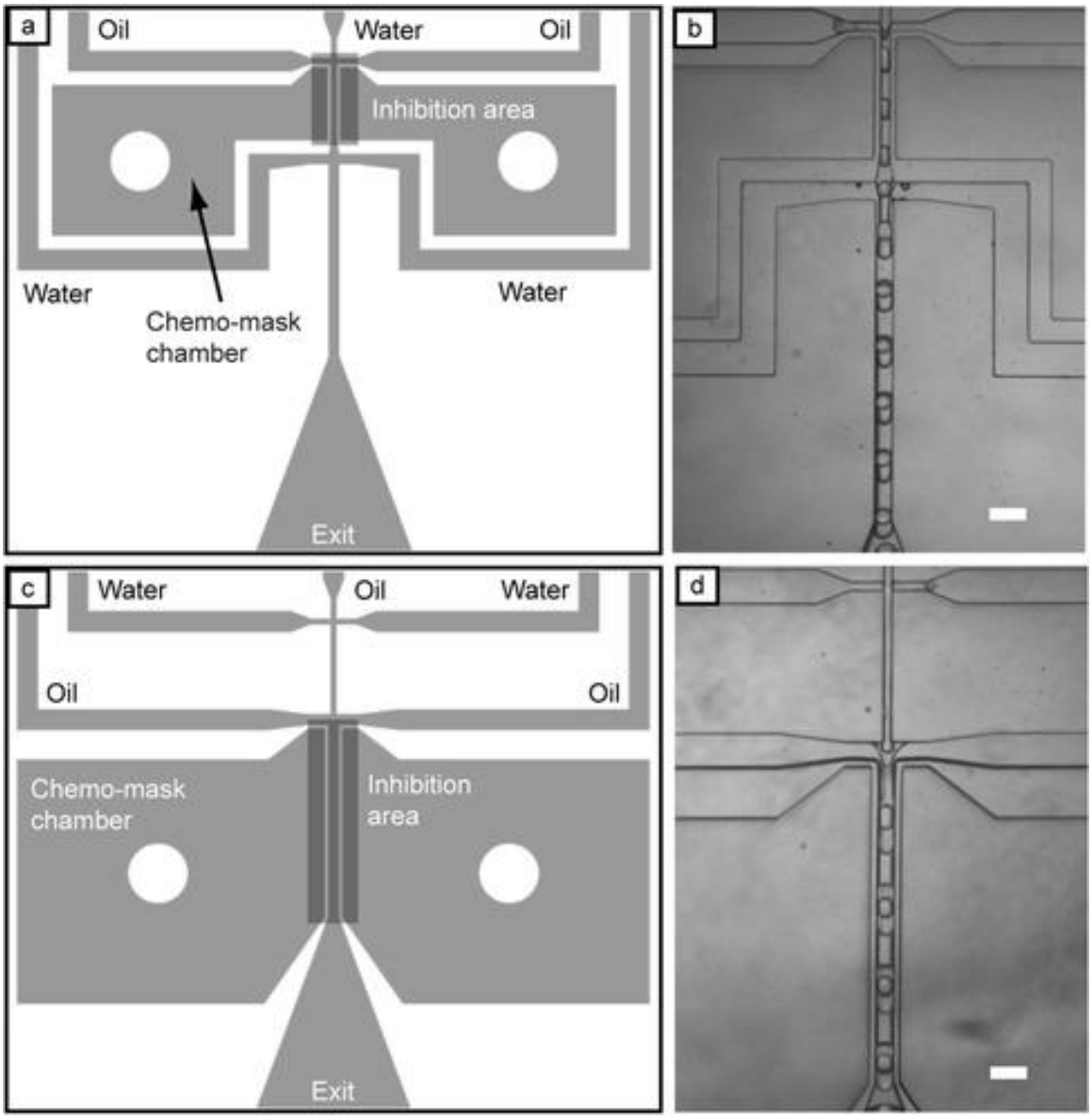

Figure 3.4: Schematics of double emulsion devices, and micrographs of the double emulsions produced, in devices made with chemo-masks and photopolymerized poly(acrylic acid), of water-oil-water (a, b) and oil-water-oil (c, d) types. The shaded channel segments in (a, c) grow no polymer , due to the chemo-masks, and thus remain hydrophobic; the rest of the channels become hydrophilic. The circular support posts stabilize the roofs of the chemo-mask chambers. In both devices the flow rates are 300 μL h^{-1} in inner phase, 600 μL h^{-1} in middle phase, and 1000 μL h^{-1} in outer phase. Scale bars denote 100 μm.

emulsion drops at flow rates of 300/600/1000 mL h^{-1} for inner/middle/outer phase. Each oil phase is the fluorocarbon oil HFE-7500 with 1.8% (w/w) of a surfactant, the ammonium salt of Krytox 157 FSL oil [53], and each water phase contains the surfactant Zonyl FSN- 100 at 0.5% (w/w), or poly(vinyl alcohol) at 5% (w/w).

3.2.4 Non-photo-activated surface chemistry

An important advantage of our method over photo-mask methods is that the chemo-masks determine the polymer growth pattern independently of the source of radicals. By contrast, a photo-mask controls the locations where radicals are available, and the radicals in turn control polymer growth. Because the chemo-mask method separates the radical production process from the patterning process, non-photo-initiated polymerization may be patterned in the same way as photo-initiated polymerization. Functionally patterned devices may thus be made without any kind of photochemistry.

To show this chemical generality, we fabricate devices using the same double emulsion design as in Figure 3.1 a, but with an alternate surface chemistry, using a non-photo-activated initiator. In the alternate sol-gel coating, we include a silane methacrylate instead of the photo-initiator-silane. The methacrylate groups provide double bonds onto which a polymer chain can anchor. The sol-gel solution comprises tetraethylorthosilicate, methyltriethoxysilane, 3-(trimethoxysilyl)propylmethacrylate, water adjusted to pH 2 with HCl, and ethanol, mixed $1:1:1:1:2$ by volume; we preconvert, dilute $1:10$ with methanol, and apply to the device as described [48]. The corresponding monomer solution is an aqueous solution of the monomer, acrylamide, at 2% (w/w), and ammonium persulfate (APS) at 0.1% (w/w) and tetramethylethylenediamine (TEMED) at 0.5% (v/v), which together initiate the growth of polyacrylamide on the channel walls. We inject this monomer solution into the

coated devices and incubate overnight. To prevent solvent evaporation, we place the whole chip in a glass beaker and cover with more monomer solution. The polyacrylamide grows everywhere, turning the channel walls hydrophilic, except near the chemo-masks; after incubation we purge with air to remove unbound monomer. The resulting device produces water-oil-water double emulsions (Figure 3.5).

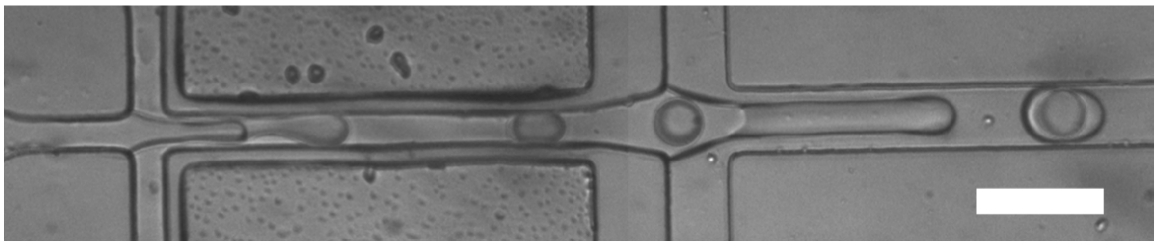

Figure 3.5: Micrograph of double emulsion production, in a device made with chemo-masks using the non-photo-based surface chemistry described in the main text. Water-in-oil-in- water double emulsions have cores of deionized water and shells of HFE-7500 with 1.8%wt Krytox surfactant, and are dispersed in aqueous solution of poly(vinyl alcohol) at 5%wt. Scale bar denotes 100 μm.

3.3 Conclusion

Our chemo-mask method makes the functional patterning of PDMS microfluidic devices simpler and more robust than standard photolithographic methods and should facilitate the fabrication of large and complex parallelized devices. Chemo-masks only modestly increase the footprint of typical devices; the chambers can be irregular or non-convex shapes, as is shown in Figure 3.1, allowing them to use otherwise unused area for oxygen reservoirs. They should be simple to include in arrays of 100 or more devices per 300 wafer. The chemo-mask method is suitable for spatial control of any kind of radical polymerization, and therefore enables non-photo-based patterning, widening the range of possible surface chemistries for microfluidics while also eliminating the need for costly UV lamps and optics. Finally, if chemo-masks are

placed above and below as well as beside flow channels, it should enable patterning of three-dimensional, non-planar shapes, in a single exposure; such patterning would be prohibitively difficult or impossible with a photo-mask.

Acknowledgements

This work was supported by the Massachusetts Life Sciences Center, BASF, the NSF (grants DBI-0649865 and DMR-0602684), the Harvard MRSEC (grant DMR-0820484), and the Brandeis NSF MRSEC (grant 0820492).

Appendix - AutoCAD files used in this work

Designs for devices shown in "Functional patterning of PDMS microfluidic devices using integrated chemo-masks", by M. B. Romanowsky, M. Heymann, A. R. Abate, A. T. Krummel, S. Fraden, and D. A. Weitz, 2010.

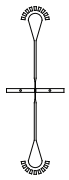

Length 200 micron (Fig. 1b)

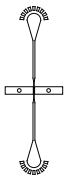

Length 400 micron (Fig. 1c)

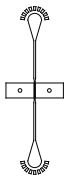

Length 800 micron (Fig. 1d)

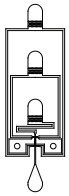

Water/oil/water device (Fig. 2a-b)

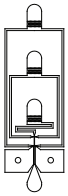

Oil/water/oil device (Fig. 2c-d)

Chapter 4

Microfluidic multiplex dialysis chip for mapping phase diagrams with reconfigurable chemical potential

Michael Heymann, Markus Ludwig, and Seth Fraden

Abstract

The Phase Chip compartmentalizes protein crystallization trials into nanoliter sized emulsion droplets and can screen up to several thousand kinetic crystallization pathways in parallel, while consuming nano-, or even picoliter amounts per sample well. Here we introduce a new Phase Chip design that utilizes a dialysis membrane, which greatly extends the range of applications, as any solute smaller than the molecular weight cut-off of the membrane can be dialyzed into and out of the sample wells. The chip is operated by controlling osmotic and hydrostatic pressure to regulate transport fluxes across the membrane. Because of its modular design, we can reuse the chip

multiple times and also harvest crystals from the chip for structure determination by x-ray diffraction.

4.1 Introduction

Microfluidic technology allows for exceptional control of solution conditions in space and time, which has been exploited to map phase diagrams [54]. In particular, crystallization in microfluidic devices has been thoroughly investigated [7, 8], and references therein. In all these microfluidic approaches to crystallization and in particular with respect to protein crystallization however it was neglected that crystal nucleation and crystal growth require opposing degrees of supersaturation [1]. To decouple nucleation and growth by means of controlling the chemical potential in the crystallization trial the Phase Chip has been developed [9, 21]. In the Phase Chip, crystallization trials are compartmentalized into nanoliter sized emulsion droplets and several thousand kinetic crystallization pathways can be screened in parallel, consuming only nano-, or even picoliter amounts per sample well. While the Phase Chip technology has successfully been demonstrated, the current permeation design is limited in two ways. The storage layer and the gradient layer are built from separate PDMS pieces, which are covalently bonded together. Thus, chips are single use only. Because chemical coupling takes place across a PDMS membrane, the flux between storage and gradient layer is limited. Small non-polar molecules permeate quickly, but water permeates very slowly and charged molecules do not permeate at experimentally relevant timescales [9, 55]. These poor transport characteristics favor very thin PDMS membranes that are very fragile and often rupture causing failure of the chip. To overcome these limitations we replaced the PDMS membrane with a regenerated cellulose dialysis membrane (Figure 4.1). Here solute exchange is limited only by the molecular

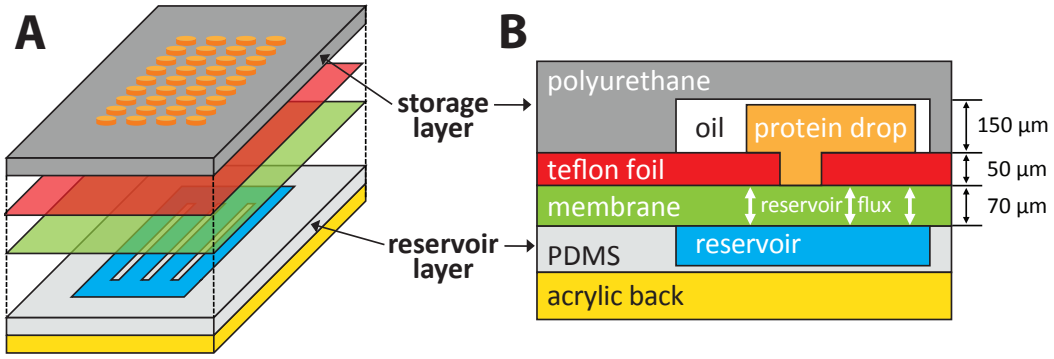

Figure 4.1: (A) Schematic overview of the dialysis Phase Chip and (B) cross-section of a single storage well. Our dialysis Phase Chip consists of two microfluidic layers that are separated by a semipermeable dialysis membrane and a perforated Teflon foil for wetting control. The storage layer on top is a matrix of a few hundred and up to a few thousand storage wells that each can hold an isolated protein solution sample. The sample droplets can interact osmotically through the dialysis membrane with the solution perfused in the reservoir layer located at the bottom of the chip. Water and solutes can exchange between sample droplet and reservoir across the membrane.

cut-off level of the chosen membrane, and ions, acids, bases or bigger molecules such as pH-buffers or even polymers can diffuse across the membrane.

Dialysis has already been achieved in microfluidic devices in general [56, 57, 58, 59, 60] and also to crystallize proteins [61], but none of these previous works have throughly characterized transport fluxes across the membrane. Because of the continuous standing column of water in a dialysis membrane, pressure gradients across the membrane can equilibrate through reverse osmosis. This makes it difficult to dialyze nanoliter volumes in parallel. In our device we can exploit osmosis and reverse osmosis to continuously and reversibly re-formulate each crystallization cocktail. We can also decouple protein crystal nucleation and growth, by first quenching into a deep supersaturation and then quench back to a low supersaturation. The chip is a clamped assembly, where the storage layer is made from polyurethane and the reservoir from PDMS. The flexible PDMS reservoir is mechanically supported by a plexiglass bottom piece to provide a good seal. Because of this modular design where both layers

are clamped together, rather then covalently combined, chips can be reused multiple times.

4.2 Device fabrication and assembly

The dialysis Phase Chip is built by combing standard soft-lithography and replica molding with custom laser cut parts. For fabricating the storage layer, we manufactured an 'inverse' negative resist master where the features are wells surrounded by higher SU8 resist. We mounted this wafer into an acrylic casting frame (Figure 4.2, A1 and C) to cast a PDMS replica that can act as a mold for the polyurethane resin (Crystal Clear 204, Smooth-On, Inc.), which after curing formed the storage layer lid. For easy chip-to-world interfacing we inserted 300 μm inner diameter polyether ether ketone tubing (PEEK tubing, from Cole Parmer) into the PDMS mold, so that it became embedded into the polyurethane piece (Figure 4.2, A2). For this we punched through holes into the PDMS mold using a 0.75 mm biopsy punch (Uni Core, Harrison) and inserted the tubing into these holes to seal off and prevent resin from flowing into the tubing. A small knot in the tubing helped to firmly embed it into the storage lid. The PDMS mold was then degassed in a desiccator for 30 mins, before the polyurethane resin was cast into the mold. We then further degased until all air-bubbles trapped in the resin had moved to the surface. Usually this was after about 1 hr. We then opened the desiccator and gently popped remaining bubbles using a Pasteur pipette, or a stream of compressed air. We let the polyurethane cure in the oven at 80 ℃ over night. After removing the cured polyurethane top from the cast, we drilled through holes and trimed the dangling end of the tubing. After a quick clean of the device with compressed air, we plasma activated the polyurethane at 500 mTorr ($\pm$ 50 mTorr) O_2 plasma at 60 watt for 1 minute, before dip-coating the

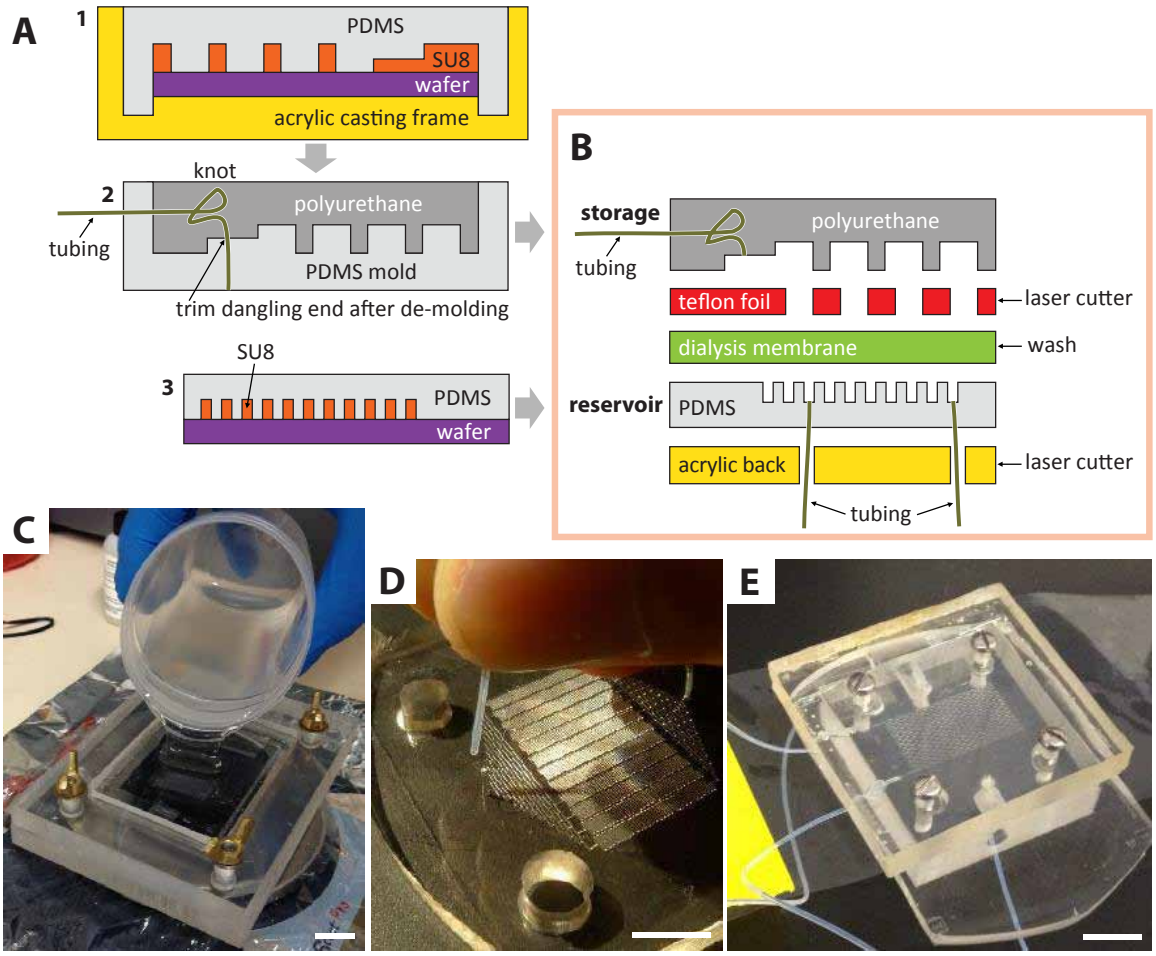

Figure 4.2: Schematic overview of fabrication workflow (A1-3) with the final assembly (B) highlighted in the red bounding box. In the first step, we prepared a PDMS mold (A1 and C) so that we could later cast the polyurethane storage lid (A2). We directly casted the tubing for interfacing with the storage layer into the polyurethane. The dangling end was trimmed later. The reservoir was directly molded from a SU8 master (A3). Here we inserted tubing directly into the PDMS reservoir (D) and wound the tubing through the acrylic back. (E) Top view of final chip assembled with four screws. Scale bars 1 cm.

lid in a 1:50 dilution of Cytop 109 AE in CTsolv 100E (both Bellex International). Cytop is a fluorophilic coating that prevents protein unfolding on the channel surface. To fully cross-link the Cytop to the polyurethane surface, we incubated the lid in the oven at 100 ℃ over night.

The wetting control layer was cut from a 50 μm thick fluorinated ethylene propy-

lene (FEP) foil (McMaster Carr) using a VLS3.50 Versa laser cutter with 50 watt Imaging Cartridge with High Power Density Focusing Optics (HPDFO).

The PDMS reservoir was cast on a traditional SU8 master, where features built up as posts defined the channels in the PDMS piece (Figure 4.2 A2). To interface into the PDMS reservoir, we punched through-holes using a 0.75 mm biopsy punch (Uni Core, Harrison) and directly inserted the tubing into the holes (Figure 4.2 A3).

The 73 μm flat sheet regenerated cellulose dialysis membrane with 6000 molecular weight cut-off (Bel-Art Products, Peaquannock, NJ) was incubated for 15 min in ultrafiltered water (Millipore Elix 3) to wash away glycerol and other additives used for storing the membrane. We then washed again for 15 min in 10 mM EDTA to remove residual metal ions.

The acrylic back was cut to shape using a VLS3.50 Versa laser cutter with 50 watt Imaging Cartridge with HPDFO and then manually threaded so that four screws could pull the chip-sandwich together.

To assemble the chip (Figure 4.2 E), we positioned the interfaced PDMS reservoir layer on the acrylic back. The rinsed dialysis membrane of desired pore-size was then gently dried using Kimwipe tissues such that the membrane was moist inside, but no water puddles remained on its surface. We dispensed 100 μl FC-43 (Sigma Aldrich) onto the dialysis membrane before depositing the wetting control layer on top. Another 100 μl FC-43 were dispensed onto the FEP foil before placing the polyurethane storage layer on top. The FC-43 oil lubricated the FEP foil, so that it could be easily aligned later. We inserted the screws to clamp the sandwich together, aligned the wetting control layer with the storage lid and finally tightened the screws until the features in the PDMS reservoir layer were barely beginning to distort from the pressure. We finally primed the chip by dead-end filling the aqueous reservoir solution into the reservoir and 12 wt% Fluorooctanol in FC-43 into the storage layer

until no air-bubbles remained trapped in the chip. After each use, all components were washed in a sonicator bath with 1 vol% Helmanex and 1 wt% Zonyl FSN-100 fluorosurfactant for 15 minutes, then repeatedly rinsed with ultrafiltered water, dried with compressed air and stored away for reuse.

4.3 Loss-free sample loading using capillary valving

We stored the sample in cylindrical wells. All storage wells were connected in series by a continuous serpentine channel through which one well was loaded after the other (Figure 4.3). To eliminate sample loss from channel dead-volume, we exploited the capillary valve based "store-then-create" loading technique [62]. In brief: The chip was primed with a fluorinated oil before the aqueous sample was injected into the device. The surface tension at the oil-water interface between priming oil and aqueous sample resulted in a pressure difference across the interface. This Laplace pressure can be calculated by the Young-Laplace equation as

$$\Delta P = \epsilon \left(\frac{1}{R_x} + \frac{1}{R_y} \right), \tag{4.1}$$

with R_1 and R_2 as the main radii of curvature and ϵ being the surface tension of the interface. To minimize its energy, the interface has to minimize its surface which is equivalent to maximizing its main radii of curvature at constant volume. A low curvature interface in a wide channel has a lower Laplace pressure then a high curvature interface in a narrow channel segment. Therefore, the sample plug preferentially entered and flowed through the wide bypass channel instead of flowing through the narrow capillary valve channel (Figure 4.3). The sample plug was then followed again

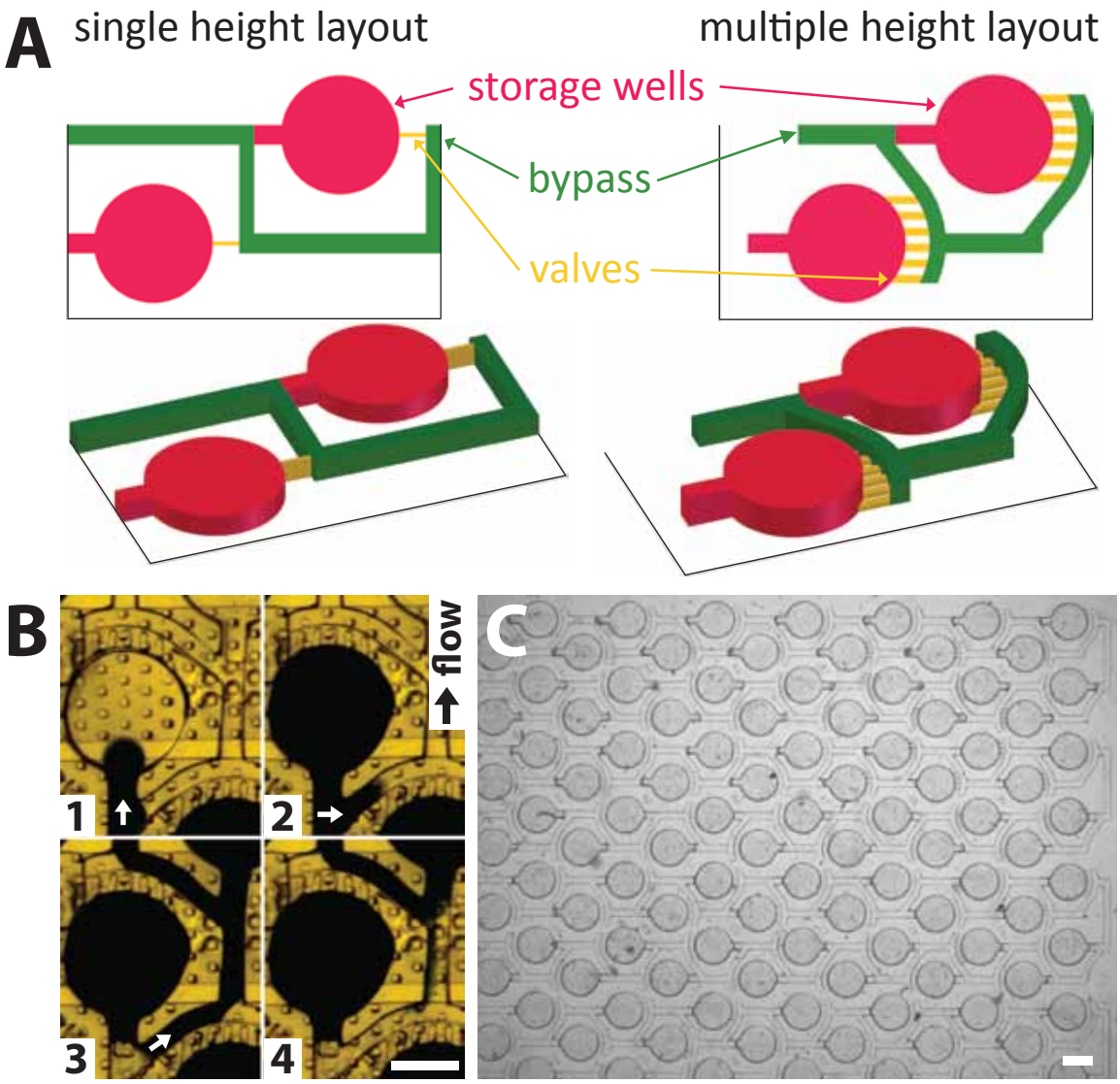

Figure 4.3: (A) Schematics of alternative Phase Chip storage layers for the single height design (left) and the multiple height multi-valve design (right), as viewed from top and from the side. (B) Image sequence of an aqueous solution of food dye loaded into the storage layer. Channel cross-sections (height · width) of the device used here are bypass = 100 μm · 100 μm, storage well entry = 150 μm · 100 μm, and valves = 25 μm · 80 μm. The chip was primed with 12 wt% Fluoro-octanol in FC-43, before blue food dye was injected into the storage wells. The flow rate was 150 $\mu L/hr$ throughout the experiment. White arrows indicate the direction of flow. Scale bar 300 μm. (C) Top view of loaded device with all visible 98 wells loaded defect free, illustrating robust sample loading. Scale bar 500 μm.

by oil, which separated the sample in the wells into independent droplets.

Compared with the previous design [21], we improved the Phase Chip storage layout in several ways (Figure 4.3 A). First, we routed the bypass closer around the wells to condense the design. By this we increased the well density by 27%. Second, we made the chip manufacturing more robust by replacing the fragile thin and tall valve in the single height design with a shallow and wide valve in a multi height design. While not changing the actual cross-section of the valve, this greatly improves master durability and also allowed us to cast plastic chips from silicone rubber molds. Third, we improved loading efficiency by introducing multiple parallel valves. This, in analogy to electric resistors connected in parallel, reduced the hydrodynamic resistance of the valve section and allowed us to load the chip reliably with flow rates of up to 150 $\mu l/hr$, which was a more then a 3 fold increase over the single valve design.

4.4 Operating the device: Interplay of osmotic and hydrostatic pressure

Osmosis is the equilibration of the chemical potential of two solutions with different concentration by the net movement of solvent through a semipermeable membrane. The osmotic pressure in turn is the pressure required to prevent the flow of solvent from low to high concentration c solution across the membrane, with:

$$p = c \cdot R \cdot T, \tag{4.2}$$

where n is the number of molecules, V the Volume, $R = 8.3144621 \frac{J}{molK}$ the gas constant and T the temperature. The osmotic pressure depends only on the osmolarity $c = \frac{n}{V}$, but not on the nature or size of the molecules. When the applied

pressure becomes larger than the osmotic pressure, the solvent can be forced to flow against the chemical potential (i.e. concentration) gradient, which is known as reverse osmosis.

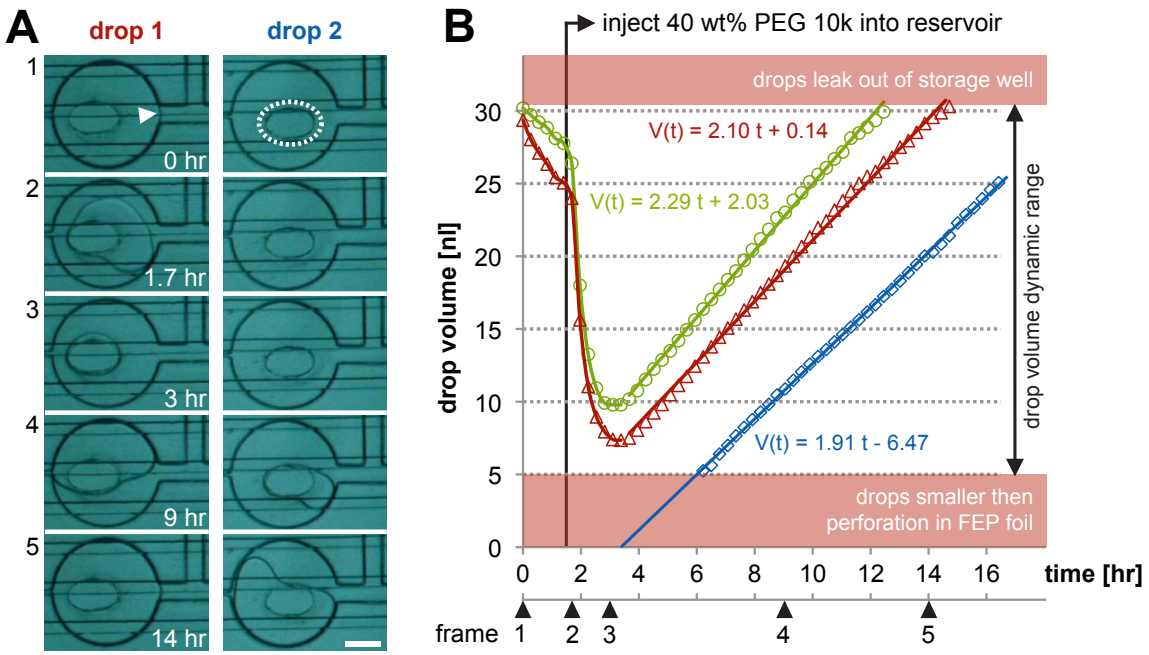

Figure 4.4: (A) Snapshots of droplet size change and (B) measured drop volume change over time when stored droplets containing 20 wt% PEG 10000 were osmotically quenched against 40 wt% PEG 10000 injected into the reservoir layer at a constant flow rate of 150 $\mu l/hr$. For this we converted drop area into drop volume as described in the main text. Droplets initially filled the well completely, but then shrank to a little less then a third of their initial volume. All droplets reached their smallest volume after 2.5 hrs, or about one hour after injection of 40 wt% PEG began. From 2.5 hrs onwards we observed drop volume to increase again, at a constant rate of about 2 nl/hr. Linear trendlines were fitted to the trajectories beginning after 2.5 hrs. Note that even drop 2 (blue diamonds) which did not fill during the loading swelled at a constant rate. We first observed a small aqueous droplet to appear in well 2 after 4.3 hrs, but only computed its volume after it had outgrown the size of the perforation in the FEP foil (A, dashed ellipse in frame 1). Scale bar 200 μm.

To test on-chip osmosis, we concentrated a stored sample of 20 wt% PEG 10000 molecular weight by placing 40 wt% PEG of same molecular weight into the reservoir (Figure 4.4). By using cellulose membrane sheets with 6000 molecular weight cut-

off (Bel-Art Products, Peaquannock, NJ), we minimized exchange of PEG across the membrane. First, we equilibrated the reservoir layer with 20 wt% PEG 10000 molecular weight for half an hour at a flow rate of 150 $\mu l/hr$. We then injected 20 wt% PEG 10000 into the storage layer at a flow rate of 50 $\mu l/hr$, while keeping the reservoir running at a constant 150 $\mu l/hr$. Then we injected oil with 4000 $\mu l/hr$ for 25 s to completely flush out tiny aqueous droplets from the storage layer bypass channel. Finally, we decreased the oil flow rate into the storage layer to 20 $\mu l/hr$ for the remainder of the experiment and began recording images (t = 0). About 1.5 hrs later, we started injecting 40 wt% PEG into the reservoir at 150 $\mu l/hr$.

To convert drop areas into volumes, we limited the contact zone of each storage well with the dialysis membrane to about a sixth of the total size of each well. Knowing the height of the device, we could approximate the drop volume as drop area times well height plus area of perforation times FEP foil thickness. In our case each droplet had about 30 nl total volume.

We observed all droplets to change their volume throughout the experiment (Figure 4.4). Droplets quickly shrank to about a third of their initial volume when the high PEG solution was injected into the reservoir. From about 2.5 hrs onwards all droplets, even initially empty ones (Figure 4.4, drop 2), kept swelling at a constant rate of about 2 nl/hr for the remainder of the experiment, even though flow rates were not changed.

This linear response let us hypothesize that water was pushed from the reservoir, which was injected at a constant flow rate of 150 $\mu l/hr$, across the membrane into the droplets in the storage layer, where oil was injected at a lower flow rate of 20 $\mu l/hr$. The gradient in flow rates could have resulted in a gradient in hydrostatic pressures, with the higher flow rate corresponding to higher pressure. The pressure gradient would then have pushed the solution from the reservoir against the concentration

gradient into the storage well. Under such a scenario, the flux would have been constant, as the flow rates and thus the pressures were kept constant.

This hydrostatic pressure reasoning could also explain the artifacts at the beginning of the experiment. During loading we operated the device with 150 to 50 $\mu l/hr$ reservoir to storage layer. Reverse osmosis during this time could have diluted the PEG concentration stored in the wells from 20 wt% down to around 13 wt% PEG, which when exposed to 40 wt% PEG would shrink to a third of the volume. We also noted unusually many small aqueous droplets flowing in the bypass channel after re-injecting oil to cut the sample drops apart. A few such droplets are common and can form spontaneously when the sample plug enters the storage layer. Here it is likely that droplets already swelled out of the storage well before loading was completed. If the drop became large enough to block the bypass, the dangling end would pinch off, as oil was flowing constantly. Quickly purging the bypass with a very high flow-rate of 4000 $\mu l/hr$ for about half a minute could have altered the net pressures over the membrane, such that solvent was pushed up into the storage layer. Concomitantly, we note a small shrinking of the PEG drops in the first 1.5 hrs, when no osmotic gradient was present yet. However, a full quantitative analysis was not possible. We speculate that when flow rates are changed, pressures equilibrate only slowly, especially when a large excess pressure has build up and is stored in compliant deformation in the microfluidic chip.

4.4.1 Hydrostatic pressure driven trans-membrane flux with blocked outlets

To determine water flux through the dialysis membrane, we quantify drop size changes as a function of absolute and relative hydrostatic pressure difference across the mem-

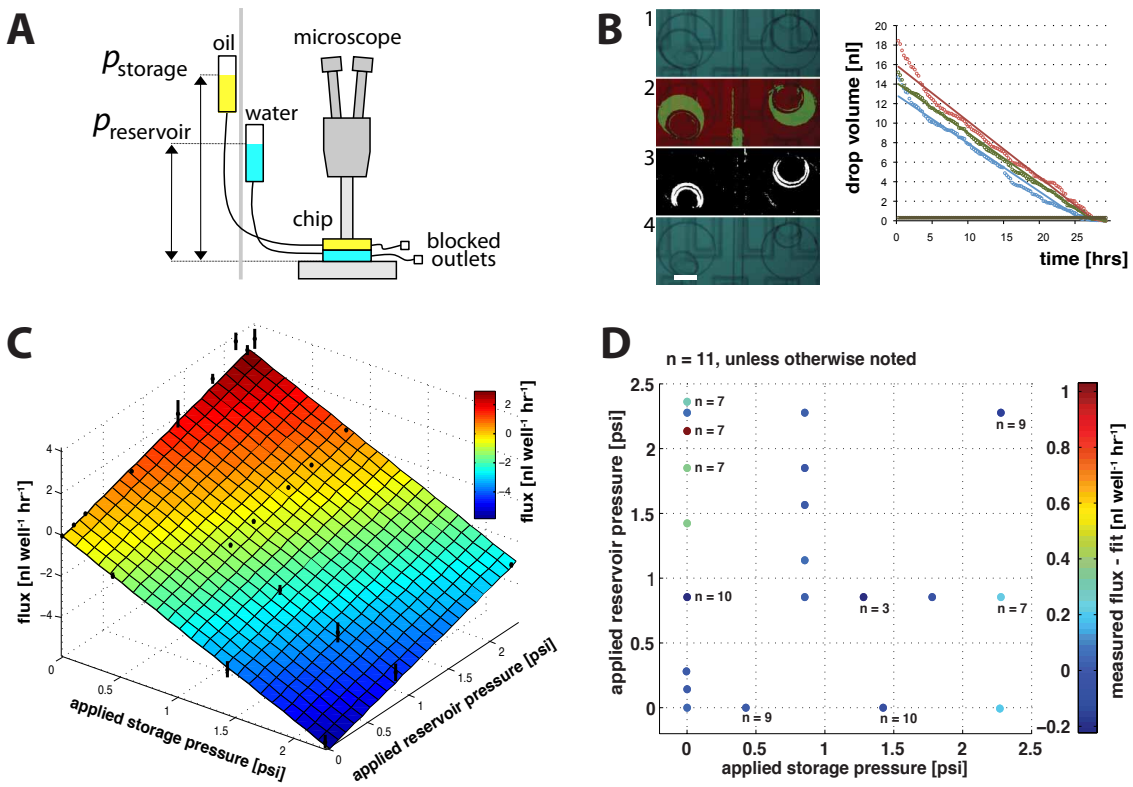

Figure 4.5: Hydrostatic pressure driven flux across the dialysis membrane with blocked outlets. (A) Schematic of experimental setup to apply hydrostatic pressures on the phase chip: Two funnels, one filled with FC-43 oil and the other with water were mounted on a stand and connected to the storage layer and the reservoir layer. The height of the vials could be varied in order to apply different pressure conditions. Both outlets were plugged. (B) Matlab image analysis to quantify drop volume: (1) First raw image in time lapse data series: Circumference of the droplet is visible. (2) Recognized edges for each frame. (3) Volume changes were quantified by first adding up all edges detected in each frame (green areas). From this template the moving edge was then subtracted for each frame. (4) final raw image of image series. For each measured rate a total of 7 to 11 trajectories were quantified (compare n-values in D). (C) Measured transport fluxes and their standard deviations of water as a function of hydrostatic pressure with blocked outlets. All measured data points fitted onto a plane as detailed in Equation 4.3. (D) Residual errors to examine the goodness of the fit in (C). Here the fitted fluxes were subtracted from the measured rates and the differences were color coded according to the column on the right. N-values specify how many individual drop-trajectories (B) each where combined into one datapoint in (C and D).

brane (Figure 4.5). To eliminate artifacts from osmotic stress, we loaded the chip reservoir and the storage layer wells with destilled water. We then connected two vials that were open to air at the top to the chip: FC-43 oil to the storage layer and water to the reservoir (Figure 4.5 A). Because every microfluidic channel has a hydrodynamic resistance, any flow across it will cause a pressure drop along the flow direction. To minimize artifacts from pressure gradients within each chip layer we plugged both outlets. We then monitored drop volume change using time-lapse microscopy of a section in the center of the chip for a total of 21 different pressure combinations. Depending on the applied pressure, the drops grew or shrunk with time. Using Matlab image analysis we extracted drop contours and computed corresponding volumes from these area measurements. We always observed drop volume to change linear with time (Figure 4.5 B). We fitted a linear curve to usually 7 to 11 droplets each per pressure combination and then averaged all flow rates measured for a given pressure combination and also computed the standard deviation. The exact n-values are listed in (Figure 4.5 D). All 21 flux rates fitted neatly into a plane (Figure 4.5 C):

$$f(p_{storage}, p_{reservoir}) = a \cdot p_{storage} + b \cdot p_{reservoir} + c, \tag{4.3}$$

with $a = -2.48 \pm 0.06$ $\frac{nl}{well \cdot hr}$ (2.3% error), $b = 1.32 \pm 0.03$ $\frac{nl}{well \cdot hr}$ (2.4% error), and $c = -0.10 \pm 0.02$ $\frac{nl}{well \cdot hr}$ (19.9% error). All errors are standard deviations. The offset plane was a good fit for the measured flux rates, since the relative errors of the fit parameters were below 3% for a and b and below 20% for c. The parameter c represents the growth rate of the droplets at pressures of zero. c is a negative number, meaning that drops shrank when no pressure gradient was across the membrane. The parameter a represents the effect of a hydrostatic pressure in the storage layer on the

growth rate of the droplets: a was negative and thus any positive pressure would drive drop shrinkage. b is positive and quantifies the effect of increased reservoir pressure on the growth rate respectively: A hydrostatic pressure applied to the reservoir caused drop growth. These observations were in agreement with the principles of reverse osmosis. The ratio $\frac{a}{b} = -1.9$ indicates that it was easier to shrink the drops than to grow them. With the same absolute growth rates, 1.9 times more pressure was needed for growing the drops than was for shrinking them. Different values for a and b also mean that the growth rate was not only dependent on the pressure difference, but also on the absolute pressures.

4.4.2 Modeling trans-membrane flux as a resistor network

To better understand the different pressure dependencies of storage and reservoir layer, we took advantage of the analogy between electrodynamics and hydrodynamics and modeled the chip with an electric network model (Figure 4.6). The oil vial and the water vial are sources of constant pressure and were modeled as sources of constant voltage U_1 and U_3. Conservation of mass required that any amount of water entering the chip needed to displace a similar amount of oil to exit the chip. With blocked outlets and without leakage the oil would have to exit through the storage layer inlet. To infer if leakage fluxes need to be taken into account, we tested if influx and outflux match. For this, two little colored indicator drops were positioned into the two inlet tubings. Without leakage, both drops should have moved at the same velocities, one towards the chip and the other coming from the chip. We found that the flow rates of both indicator droplets differed by a factor of about 30. Thus leakage fluxes needed to be respected in our model. The leak could have either been in the storage layer or the reservoir layer, or in both. Also, the channels in both layers had flow resistances. We modeled these by R_1 and R_5 for the storage- and the reservoir

layer. The respective leaks were represented by R_2 and R_4. These two branches were coupled by the membrane which was R_3 in the model. Any current passing through R_3 has to be understood as flux of water out of or into the drops, depending on the sign.

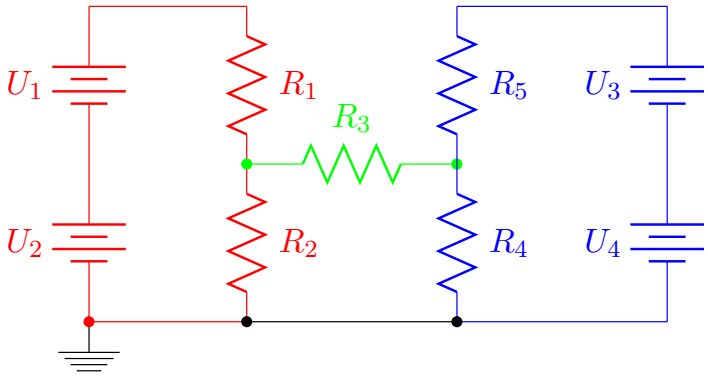

Figure 4.6: Resistive network as a model for the Phase Chip: The red branch represents the storage layer and the blue branch the reservoir layer. R_2 and R_4 model leaks while R_1 and R_5 are the respective hydrodynamic resistances of the microfluidic channels of the storage layer and the reservoir. R_3 couples both branches and thus models flux across the membrane and any current through R_3 has to be understood as flux of water across the membrane that causes the drop size to change.

To solve the system, both branches had to be connected to a common ground. Two more constant voltage sources U_2 and U_4 were added. These sources formed potentials that caused both the water and the oil to evaporate from the chip. They could be related to the solubility of oil or water into the environmental air as well as the flux of water through PDMS by diffusion. Hence, the voltages of these sources depended on the temperature as well as on the oil and water saturation of the surrounding atmosphere. According to Kirchhoff's Law we derived three equations from

the circuit:

$$\begin{aligned} -U_2 - U_1 + I_1 R_1 + R_2(I_1 - I_2) &= 0 \\ R_2(I_2 - I_1) + R_3 I_2 + R_4(I_2 - I_3) &= 0 \\ U_3 + U_4 + R_4(I_3 - I_2) + R_5 I_3 &= 0 \end{aligned} \tag{4.4}$$

A Gauss elimination yielded the current I_3, representing the flow-rate of water through the membrane:

$$I_3 = \frac{R_2(U_1 + U_2)(R_4 + R_5) + R_4(R_1 + R_2)(U_3 + U_4)}{(R_4 + R_5)((R_1 + R_2)(R_2 + R_3 + R_4) - R_2^2) + R_4^2(R_1 + R_2)} \tag{4.5}$$

Here, U_1 and U_3 were variables, while the constant parameters R_1 through R_5, U_2 and U_4 define the system. Since the fit plane was defined by three degrees of freedom, I_3 was overdefined by 4 variables. However, from Equation 4.5 we could infer that this resistive network model also yields a plane as I_3 could be simplified:

$$I_3 = A \cdot (U_1 + U_2) + B \cdot (U_3 + U_4) \tag{4.6}$$

$$= A \cdot U_1 + B \cdot U_3 + C. \tag{4.7}$$

Changes in U_1 or U_3 correspond to the different slopes A and B in I_3. Constant U_2 and U_4 add the offset C to I_3, matched with the fit parameter c in Equation 4.3. This offset at zero of the fitted plane might not only be controlled by the evaporation of water or oil. Also the Laplace pressure inside the droplets could contribute to this offset. The Laplace pressure depends on the main radii of curvature of the droplets. In the storage layer, the drops are confined to the height of the storage wells. Assuming that the drops are circular, the Laplace pressure is related to their circumference as well as to their height. When the drops shrink, their height remained constant but their circumference changed causing a higher Laplace pressure in smaller drops

compared to bigger ones. Thus, smaller drops should shrink faster than bigger drops and their volume changes over time would not be linear. As we observed all droplet trajectories to be linear, we assumed the Laplace pressure to be negligible.

4.4.3 Trans-membrane flux with open reservoir outlet

To maintain a steady state in the chip the reservoir has to be replenished constantly. Therefore, we quantified water flux through the membrane with open reservoir outlet (Figure 4.7) under either hydrostatic pressure or under constant flow driven flow.

1.) Hydrostatic pressure driven reservoir: Flow in microfluidic channels causes a pressure gradient along them. If large enough, this pressure gradient could result in a gradient of drop growth rates. To minimize such an undesired effect, we engineered the channel cross section close to the reservoir in- and outlets to be 12 times smaller than the channel cross section of the channels perfusing under the stored droplets. We used a microscope with a scanning stage to capture time-lapse movies of all drops. To test for a systematic effect across the chip, we sub-divided the whole storage array into a 8 x 8 matrix for analysis. From this matrix we selected the droplets in the top, middle, and bottom row and manually measured drop areas using ImageJ to quantify drop volumes. As in the previous experiments, we assumed that the transmembrane flux was constant in time. We thus computed the growth rate for each droplet simply as volume difference between the beginning and end of the experiment.

We observed the trans membrane flux to be less for each pressure combination when compared to the previous case when all outlets were blocked. This was consistent with the fact that the pressure drops with flow in a channel. Combining a total of five such whole-chip measurements, we could again fit a plane of form Equation 4.3 to our data, with $a = -2.06 \pm 0.05$ $\frac{nl}{well \cdot hr}$ (2.4% error), $b = 0.79 \pm 0.06$ $\frac{nl}{well \cdot hr}$ (7.0%

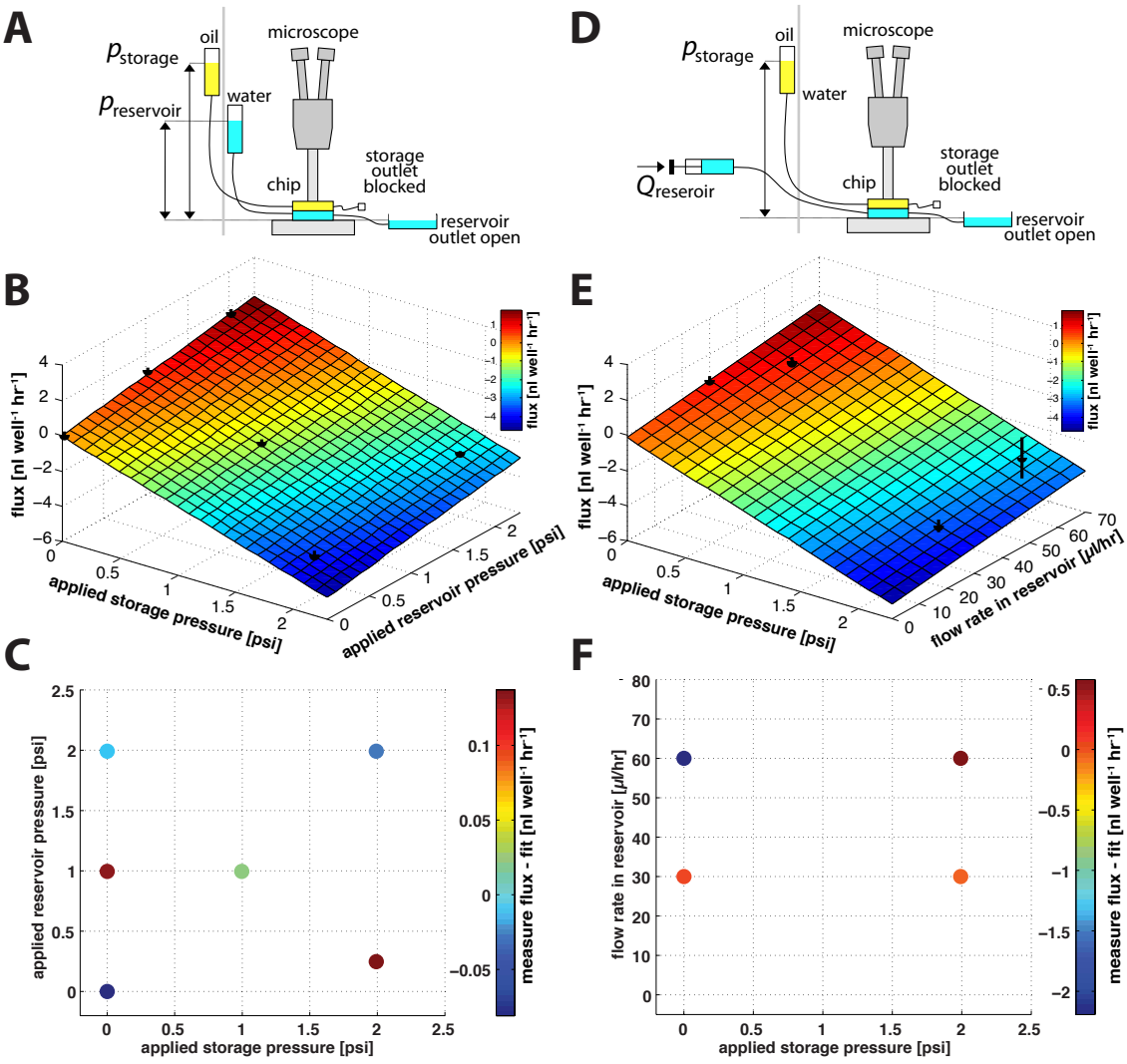

Figure 4.7: Trans-membrane flux with open reservoir outlet. (A to C) Flow in reservoir and storage layer was controlled by hydrostatic pressure. (D to F) Hydrostatic pressure controlled storage layer and constant volumetric flow in the reservoir layer. (B and E) Measured transport fluxes (half circles) and their standard deviations (error bars) of water as a function of hydrostatic pressure were fitted onto a plane of Equation 4.3. (C and F) Residual errors to examine the goodness of the fit in (B and E). In each instance, the fitted fluxes were subtracted from the measured rates and the differences were color coded according to the column on the right.

error), and $c = -0.01 \pm 0.07$ $\frac{nl}{well \cdot hr}$ (785.3% error). All errors are standard deviations. We did not observe a systematic gradient in growth rates. If present, the effect was below our analysis resolution of around $\pm$ 0.05 $\frac{nl}{well \cdot hr}$ error per drop volume measured.

However, one potentially could re-engineer the reservoir to maximize the pressure drop over the chip. Alternatively, a gradient of transmembrane flux rates could be implemented by systematically re-sizing the contact area that each droplet has with the dialysis membrane. Flux scales linear with cross-section area and therefore two-dimensional concentration gradients could be engineered this way. This could be exploited for example, by generating different rates of increasing/decreasing protein and/or polymer concentration in the rows versus a pH gradient in the columns.

2.) Constant flow driven reservoir: We then re-examined how constant flow into the reservoir (Figure 4.4) might be compensated by hydrostatic pressure on the storage layer. We modified our set-up to have syringe pump driven flow into the reservoir with open reservoir outlet. The storage layer was again controlled by hydrostatic pressure with the storage layer outlet blocked (Figure 4.7). As previously, we analyzed volume changes using ImageJ and again could fit a linear plane of form Equation 4.3 to the data points, with $a = -2.18 \pm 0.05 \ \frac{nl}{well \cdot hr}$ (5.2% error), $b = 0.02 \pm 0.006 \ \frac{nl}{well \cdot hr}$ (30.9% error), and $c = -0.1263 \pm 0.29 \ \frac{nl}{well \cdot hr}$ (231.8% error). All errors are standard deviations. In conclusion, we could control transmembrane flux by balancing flow rates and storage pressure quite well. Nevertheless, operating microfluidic devices with constant flow always beares the risk of pressures building up in the device uncontrollably. This actually happened in one of the experiments, when one of the channels clogged. After a couple of hours of shrinking, the droplets started to grow excessively. We preferred operating the device with full pressure control. However, one could include safety valves with the reservoir inlets to prevent too high a pressure building up in the chip.

4.5 Large viscosity gradients: crystallizing glucose isomerase in a PEG gradient

Viscous solutions, like polyethyleneglycol (PEG), are often used as a precipitant in protein crystallization [1]. In pressure driven flow, the flow rate Q scales with the dynamic viscosity η according to Hagen−Poiseuille as

$$Q = \frac{\Delta P \cdot \pi \cdot r^4}{8\eta \cdot L}, \tag{4.8}$$

with ΔP as the pressure difference along the channel, π as the mathematical constant pi, r the radius and L the length of the channel. Viscosity does not change linearly with polymer concentration. Therefore, a linear 'Whitesides'-gradient [63] is difficult to obtain under pressure driven flow with solutions that have very different viscosities. While the gradient generating tree could be optimized to compensate for viscosity dependent flow rates, a new gradient for any new pair of two viscosities or polymer concentrations would be required.

As a simpler alternative, we explored using a continuous single-inlet reservoir to produce static spatial concentration gradients. For this we first primed the device with one of the two buffers and then slowly injected the second buffer. While displacing the first buffer from the channels, the incoming second buffer is continuously diluted with the first buffer that was already stored in the channels and the membrane. If timed correctly one could produce a continuos concentration gradient that should be stable for a few days as diffusion of large polymers is slow.

To test this logic we used glucose isomerase, which precipitates when diluted in 40 wt% PEG 10000, 100 mM ammonium sulfate, pH 7.3 with a concentration of $\geq$

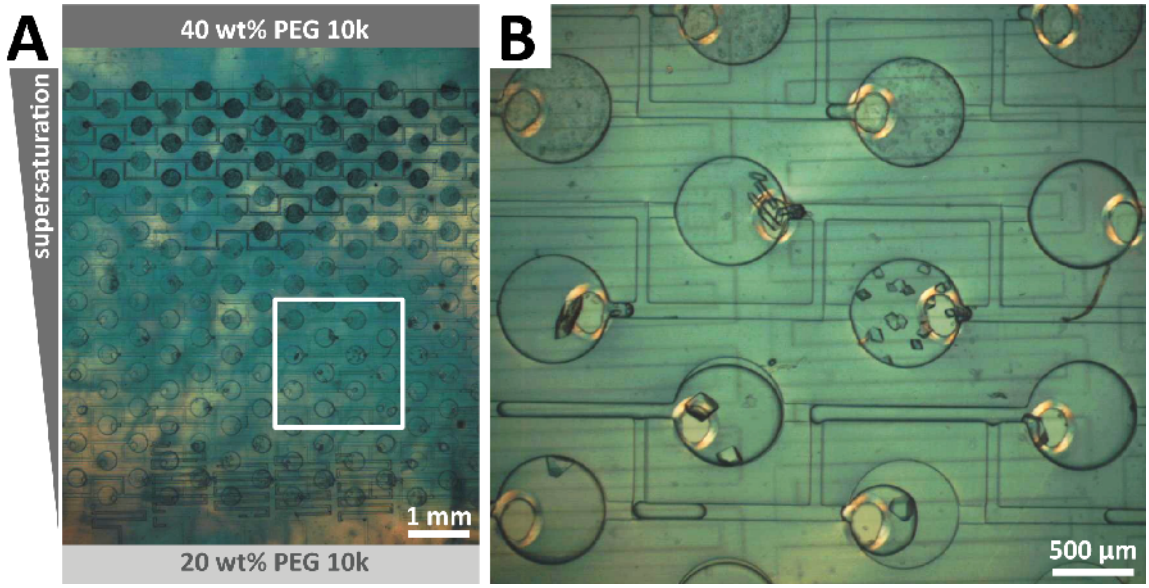

Figure 4.8: (A) 30 mg/ml glucose isomerase crystallized against a PEG gradient of 20 to 40 wt% PEG 10000 with a homogenous background of 100 mM ammonium sulfate, pH 7.3 as detailed in the main text. Notice the shallow depth of the crystallization slot, from no crystals (bottom rows), to single crystals, to multiple crystals per drop to precipitate (top rows). (B) Close up of inset in (A).

30 mg/ml. At 20 wt% PEG 10000, 100 mM ammonium sulfate, adjusted to pH 7.3 with ammonium and 30 mg/ml glucose isomerase can crystalize, but only at very low rates with a few crystals per milliliter. Thus, only very few of the nanoliter sized wells would crystalize during as long as a week. We first equilibrated reservoir and dialysis membrane against 20 wt% PEG, before 30 mg/ml protein in 20 wt% PEG buffer was loaded into the storage layer. We then slowly injected 40 wt% PEG at 50 $\mu l/hr$ until the PEG-rich buffer had filled the reservoir layer. The reservoir ran from top to bottom (Figure 4.8 A) with 10 parallel serpentine channels that merged into one inlet and outlet each. The gradient generation took about 20 minutes during which the incoming front of high PEG concentration was consecutively diluted by the low PEG solution stored in the membrane and the above wells. As a result we obtained a continuous gradient from 40 wt% close to the inlet to 20 wt% near to the outlet. After loading and gradient set-up, all inlets were plugged and the chip was

incubated in a water bath at 4 ℃. After four days we evaluated the chip and observed a gradient from no crystallization, to single crystals, to multiple crystals per drop to precipitate (Figure 4.8).

Following the gradual dilution scheme we were able to generate intermediate concentrations of PEG in the device as evidenced by the gradient in crystallization outcomes. Future work should quantitatively characterize the gradient generated as well as its evolution over time during incubation.

4.6 Assessing crystal quality

Crystal nucleation is a non-equilibrium, dynamic process and timely detection of crystal nuclei allows prompt optimization of crystallization recipes. To finely titrate our dialysis crystallization trials into the crystallization zone we need to be able to detect the smallest possible nuclei, or ideally even sub-critical nuclei, which have not yet grown larger then the critical size associated with the nucleation barrier. To identify quench profiles that yield a crystalline phase instead of a kinetically arrested gel we used Second Harmonic Generation (SHG) imaging (Figure 4.9). Crystals grown in the chip were then harvested to collect X-ray diffraction data.

4.6.1 SHG imaging

SHG [64, 65] is the emission of radiated, coherent light at exactly twice the frequency of the incident light. Non-centrosymmetric molecular polarizability can lead to SHG and thus any chiral protein crystal can give a SHG signal [65], while disordered or centrosymmetric packings of the same individual proteins cannot. These different susceptibilities, make it a powerful detection technique for protein crystals, as even microcrystals can be selectively imaged against a background of solvated protein or

amorphous protein aggregates. Exploiting the ratio of the forward-to-backward detected SHG, Wampler et al. [66] could detect sizes of green fluorescencent protein microcrystallites and derived a general theoretical detection limit for protein crystallites of down to 100 nm in diameter under low magnification with 10x objective. These are detection limits not rivaled by traditional fluorescent, or polarization microscopy methods. Also, usually protein aggregates in solution produce substantial background fluorescence, but no detectable SHG. Similarly, salt crystals are birefringent too, but do not show SHG.

SHG is a scattering process, so there is no bleaching and because it is a 2-photon effect, there is no background SHG. The SHG signal from a protein arises primarily from the amide transition of amino acid residues. Summing the individual hyperpolarizability terms over all residues yields the SHG susceptibility tensor of a single protein [67]. From the SHG susceptibility of a single protein the SHG signal from a protein cluster can be calculated [64, 65].

Glucose isomeraze crystalizes with orthorhombic symmetry in the space group I222. It is known to have a good SHG signal [68]. We grew crystals by loading 30 mg/ml glucose isomerase at 20 wt% PEG 10000, 100 mM ammonium sulfate, pH 7.3 and subsequently quenching the whole chip to 30 wt% PEG 10000, 100 mM ammonium sulfate, pH 7.3. We then sealed all outlets and incubated the chip in a

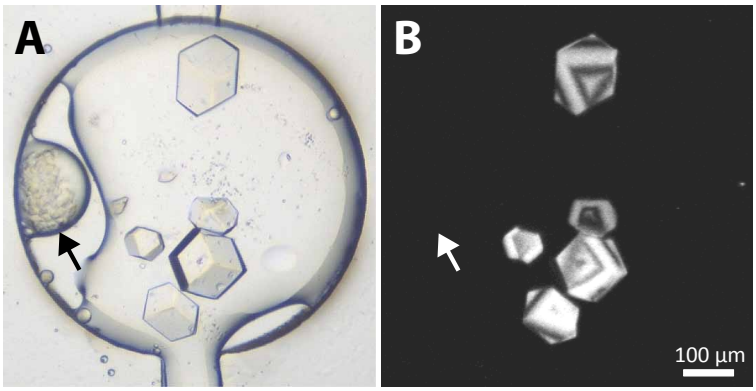

Figure 4.9: Glucose isomerase crystals in the dialysis phase chip imaged with (A) bright field microscopy and (B) with SHG. The arrow indicates non crystalline protein aggregates that have no SHG signal.

water bath at 4 ℃ for several days. Crystals were observed inside the chip using bright field microscopy and SHG imaging (Figure 4.9), using the SONICC imaging platform (Formulatrix, Waltham, MA) with 10x objective. Glucose isomerase crystals gave strong SHG signal, while no SHG signal was observed from amorphous aggregation found in a few wells. We did not detect significant background from the chip in SHG. We concluded that the chip with its different components is well suited for SHG imaging.

4.6.2 Harvesting crystals for X-ray crystallography

To mount crystals for cryo crystallography we carefully opened the chip, by gently pressing the lid down while removing all four screws. We then took the storage lid off the chip and applied 1 ml 40 wt% PEG 10000, 100 mM ammonium sulfate, pH 7.3 onto the lid and also onto the teflon foil and dialysis membrane left behind on top of the reservoir, as crystals stayed on both halves (Figure 4.10 A). The 40 wt% PEG buffer was used as a cryo protectant and also to keep the crystals moist for the duration of the looping.

In our FC-43 oil with 12 wt% fluorooctanol system, emulsion droplets were not stable against coalescence. Opening the chip and deposition of new buffer disrupted the emulsion stored in the chip. We found some crystals to remain in the stored wells, or attached to the teflon foil, while other crystals were freely floating in the puddle of cryo-protectant covering the chip.

We looped crystals using standard Nylon loops (Hampton Research) (Figure 4.10 B). Looped crystals where immediately cryo frozen by plunging into liquid nitrogen. Crystals remained stored in liquid nitrogen until X-ray diffraction data was collected at the MacChess F1 beam line at Cornell University in a cryostream (N_2(g)) (Figure 4.10 C&D). We took 40 consecutive frames with 1° rotation and 1 second exposure

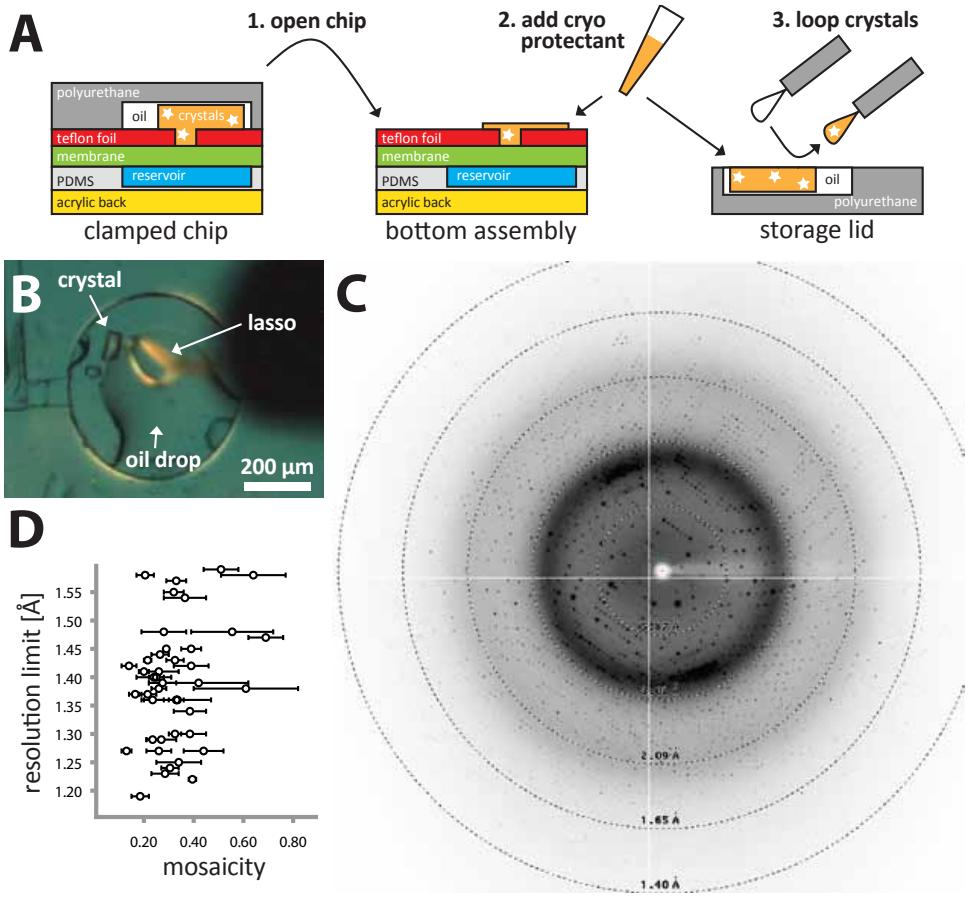

Figure 4.10: (A) Schematic of crystal harvesting from the dialysis Phase Chip. After opening the chip we add excess of cryo-protectant to keep crystals moist. (B) We looped crystals using standard nylon lassos. (C) Representative 1s exposure diffraction data set of a glucose isomerase crystal looped from the dialysis Phase Chip that was cryo-frozen in liquid nitrogen. The crystal diffracted down to 1.17 Å and had a mosaicity of 0.15 to 0.22 for the 40 frames taken with 1° rotation each. (D) Scatter plot of resolution and mosaicity for the 46 crystals harvested form the chip. Most crystals diffracted to better then 1.5 Å resolution and fell into a range of mosaicities between 0.2 and 0.4.

for a total of 46 crystals. Most crystals diffracted to better then 1.5 Å resolution. We defined the resolution cut-off to where the Bragg peak intensity dropped below twice the background intensity. The mosaicities for the crystals in our data set fell into a range of 0.2 and 0.4. The best crystal in the set had a diffraction better then the edge of the detector at 1.17 Å with mosaicity of 0.15 to 0.22.

Even though our approach to open the dialysis Phase Chip resulted in mechanical disruption of the emulsion droplets and hence the crystals in them, we could consistently loop high-quality crystals for X-ray crystallography from the chip. To minimize mechanical disruption when opening the chip, the teflon sheet for wetting control could be covalently attached to the storage lid. This would ensure that droplets would stay intact when retrieving the storage lid from the chip. Each droplet could then be accessed independently.

4.7 Conclusions

We designed a new microfluidic dialysis chip, to kinetically probe phase diagrams in a high throughput manner. Exploiting osmosis and reverse osmosis, we performed proof of principle experiments crystallizing glucose isomerase. We confirm that protein crystallization can be monitored using Second Harmonic Generation and that crystals can be harvested from the chip to collect high resolution X-ray diffraction data. In current efforts we are extending the capabilities of the reservoir layer to formulate spatial concentration gradients along one [63] or two [69] dimensions, or to include formulator capabilities [9]. Ultimately we seek to apply the dialysis Phase Chip to optimize membrane protein crystallization trials with respect to optimal detergent concentration, which can not be accomplished in classic crystallization trials. We are also developing a dialysis chip compatible with polarization microscopy to be able to investigate assembly and disassembly of biological hydrogels such as intermediate filament assemblies or amyloid fibrils. With regard to protein crystallography, an X-ray transparent version of the dialysis Phase Chip would completely prevent mechanical damage to crystals during looping and freezing. Without these systematic sources for crystal damage it would be possible to directly correlate crys-

tallization conditions with crystal quality. Also, side-stepping the laborious manual crystal looping will improve throughput in data collection.

4.8 Acknowledgements

We thank Max Zieringer for technical assistance in fabricating the perforated FEP foils used in this work, Formulatrix for letting us use their SONIIC instrument to capture SHG images, Kelsey Anthony for helping with the glucose isomerase purification, and Daniel Pommeranz Krummel, Sol Gruner, Jeney Wierman, Marian Szebenyi, Irina Kriksunov, David Schuller, Chae Un Kim, Mike Cook, and Scott Smith for help and discussions with the protein X-ray crystallography. This work was supported by the NSF MRSEC (DMR-0820492) and NSF MWN 1209518. CHESS is supported by the NSF & NIH/NIGMS via NSF award DMR-0936384, and the MacCHESS resource is supported by NIH/NIGMS award GM103485.

Chapter 5

In-situ protein crystal X-ray diffraction

Michael Heymann, Achini Opthalage, and Seth Fraden

Abstract

We developed an emulsion based crystallographic technology in which nanoliter sized droplets of protein solution are encapsulated in oil and stabilized by surfactant. We exploit a confinement based feedback mechanism to decouple crystal nucleation and growth to produce one crystal per drop. Using a X-ray transparent microfluidic chip we can collect X-ray diffraction data from these crystal emulsions in high throughput at room temperature. We merged many glucose isomerase crystals into one dataset to solve the crystal structure by molecular replacement, demonstrating the feasibility of high-throughput serial X-ray crystallography in synchrotron radiation.

5.1 Introduction

The transformation of a protein solution to a crystal is governed by two non-equilibrium processes: nucleation and growth [1]. Consequently, supersaturation kinetics play an essential role in crystallization and the optimal crystallization strategy should decouple crystal nucleation from crystal growth [70]. Traditionally this has been achieved by seeding [71], or by introducing nucleants [72] to catalyze formation of crystal nuclei. In another approach a microfluidic Phase Chip has been developed to finely tune solution supersaturation throughout the crystallization experiment, which allows one to constantly adjust supersaturation in order to decouple nucleation and growth [9, 21]. These earlier designed chips though were not x-ray transparent and crystals were difficult to harvest. To close this bottleneck, microfluidic crystallization platforms compatible with *in situ* diffraction have been developed [12, 73, 74, 75]. However, these approaches built and operated valves in the chip [12, 75], thus rendering them expensive and difficult to use by microfluidic laymen. Other technologies are low-throughput [74], or need a second round of scale-up to larger capillaries [73] to grow crystals sufficiently large enough to collect diffraction data.

In this work we explore the potential of using protein crystals encapsulated into nanoliter sized emulsion droplets for x-ray structure determination. This entails finding conditions on-chip for which one crystal is grown per drop [21] and then isolating hundreds of drops stored in a x-ray transparent micro-fluidic chip. We achieved formation of single crystals by exploiting an internal feedback mechanism of rapid protein depletion upon nucleation inside the emulsion droplets to reliably nucleate one crystal per drop [76]. Single, non-cryoprotected crystals are too small amd too radiation sensitive to collect a complete diffraction set. But, a full data set with high redundancy can be obtained by merging many single diffraction patterns, if the

crystals are isomorphous. As a proof of principle we solved the structure of glucose isomerase by the method of molecular replacement, using the previously determined structure [77] as a search model.

5.2 Decoupling nucleation and growth through compartmentalization

We grew single crystals per drop by exploiting an internal feedback mechanism in the emulsion droplets due to different scaling of crystal nucleation and growth rates with volume [76]. In brief, for any combination of nucleation and growth rate there is a critical droplet volume below which only a single crystals per drop can form. Below this critical size the total protein content in the drop is consumed by the growing crystal faster then what it would take to nucleate a second crystal. Due to this protein absorption into the growing crystal the supersaturation of the emulsion droplet decreases as the crystal grows, effectively decoupling crystal nucleation and growth (Figure 5.1 A).

We grew crystals in emulsion droplets stabilized against coalescence with 2 % v/v solution of PFPE-PEG-PFPE surfactant 'E2K0660' in HFE7500 fluorinated oil (from 3M). The surfactant was synthesized as previously described [79]. We produced drops in a co-flow geometry where both protein solution and buffer do not mix in laminar flow up stream of the dropmaker (Figure 5.1 B). We then batch processed emulsion droplets in capillaries (Figure 5.1 D). Nucleation can be accelerated using temperature quenches, or by slowly letting droplets shrink by evaporation of water. Once all droplets have nucleated crystals, we transfered the capillary/chip into an osmotic bath to stop evaporation.

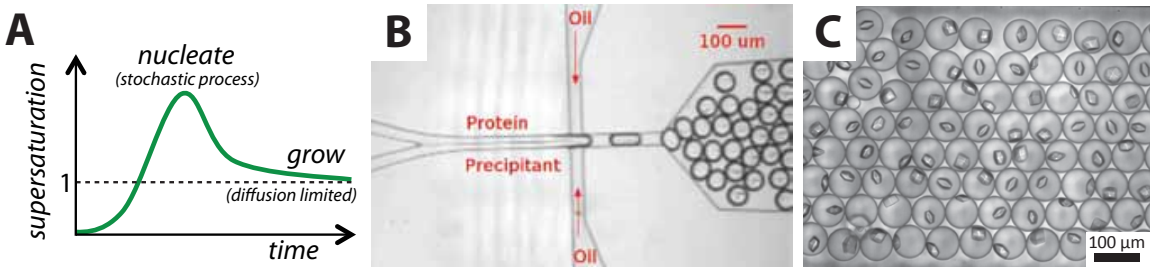

Figure 5.1: (A) An ideal crystallization trajectory increases supersaturation until just one crystal nucleates, then decreases supersaturation to prevent further nucleation, but remains mildly supersaturated to promote crystal growth. (B) We produced crystals in co-flow geometry where protein and precipitant solution did not mix in laminar flow upstream of the nozzle where both solutions became co-encapsulated into emulsion droplets. (C) Monodisperse emulsion of Lysozyme crystals. The aqueous phase of each droplet contained 30 mg/ml Lysozyme, 100 mM Sodium Acetate, pH 4.8, 12.5 wt% PEG, 5 wt% NaCl. Droplets were stored into a rectangular capillary and incubated at 6 ℃ for 36 hrs until all droplets had crystallized. (B and C) from [78].

5.3 Crystal emulsions

To confirm compatibility we tested our surfactant system with additional model proteins (Figure 5.2). In traditional vapor diffusion, a small volume of protein solution is mixed with the same amount of precipitant and then sealed into a container together with a large reservoir of precipitant. The diluted protein-precipitant drop equilibrates through vapor phase diffusion with the reservoir, resulting in a concentration increase of all components in the drop by a factor of two. We first identified a range of published crystallization recipes, which commonly were optimized to nucleate only a few crystals per microliter. Our emulsion droplets have volumes of a few pico- to nanoliter each. We therefore had to increase nucleation rates by at least two orders of magnitude. We thus prepared vapor phase and microbatch crystallization trials around the literature recipes and optimized the vapor recipes toward nucleating crystal showers of appropriate density. We desired to roughly match the number of crystals per volume in the classic crystallization methods, to the number of droplets we would

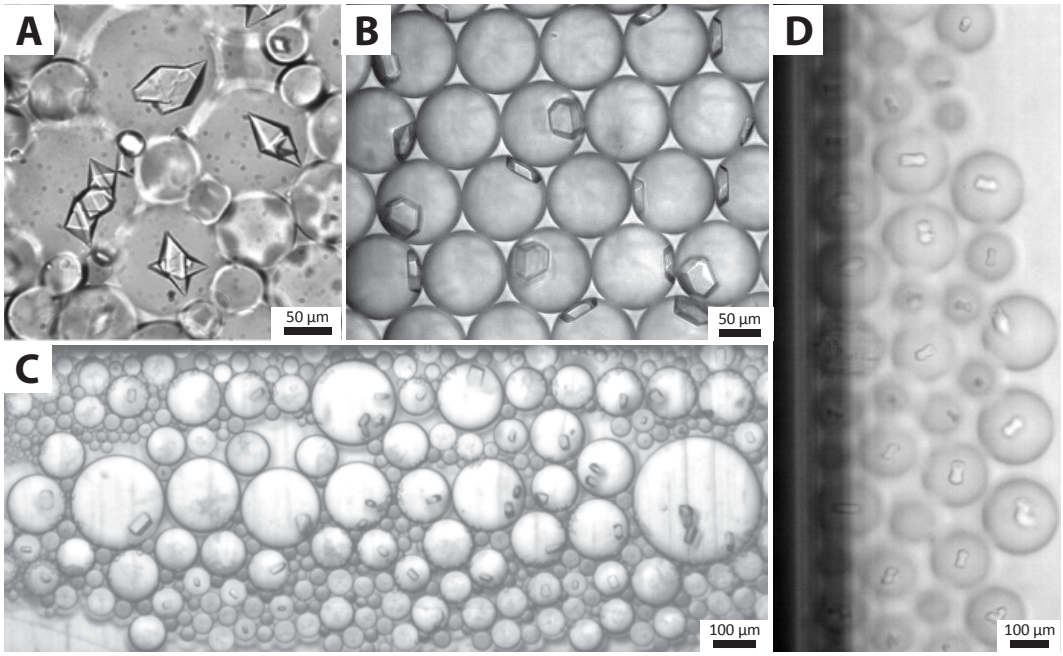

Figure 5.2: Crystallization of various proteins in emulsion droplets. (A) Trypsin, (B) Glucose isomerase, (C) Concanavelin A, and (D) D1D2. See main text for crystallization conditions.

produce from the same volume, as this would lead to about one crystal per drop. Emulsions were then prepared by mixing 2 μl protein solution with 2 μl precipitant in a PCR test-tube. Immediately after mixing, we added 30 μl 2 % v/v solution of PFPE-PEG-PFPE surfactant (E2K0660) in HFE7500 fluorinated oil. The surfactant E2K0660 was synthesized as previously reported [79]. Emulsions were formed by gently shaking the vial. Aqueous droplets were less dense then the immersing fluorinated oil, so droplets creamed to the top of the vial within a minute. The emulsion cream was then loaded into rectangular glass capillaries (Vitro Tubes) and sealed with 5 minute Epoxy to prevent evaporation. Crystallization was monitored over the course of a week. All compounds and proteins from commercial sources were used as received without further purification. The molecular weight and the net charge of the proteins during crystallization, as derived by the isolectric point are summarized in table 5.1.

Table 5.1: Properties of crystalized proteins. The theoretical pI value of D1D2 was computed using its amino acid sequence and the ExPASy ProtParam tool [80].

	formula weight	**isoelectric point (pI)**	**net charge in crystal**
Lysozyme	14.3 kDa	11.3 (from [81])	positive
Trypsin	24 kDa	10.1 - 10.5 (from [82])	positive
Concanavelin A	76.5 kDa (3mer)	4.5 - 5.5 (multiple isoforms, see [83])	negative
Glucose isomerase	173 kDa (4mer)	3.95 (from [84])	negative
D1D2	26.8 kDa (heterodimer)	10.6 (theoretical pI, from [80])	positive

Trypsin was crystalized by mixing 60 mg/ml trypsin from bovine pancreas in 10 mg/ml benzamidine, 3 mM $CaCl_2$, 0.02 wt% sodium azide with 100 mM $NaPO_4$, pH 5.9, 5.1 M ammonium acetate (all Sigma Aldrich). In this system we observed crystals in the range of pH 5.9 to pH 8.6, with higher pH values having much higher nucleation rates.

Glucose isomerase crystals were grown at room temperature (∼25℃) by preparing a crystallization batch with final concentrations of 30 mg/ml glucose isomerase from *Streptomyces rubiginosus* (from Hampton Research), 100 mM ammonium sulfate, pH 7.0, 20 wt% PEG 10,000 in a 1 : 1 ratio (all from Sigma Aldrich).

Concanavelin A was crystalized by mixing 25 mg/ml concanavelin A type IV from *Canavalia ensiformis* in 100 mM tris-HCl, pH=7.4 with 100 mM tris-HCL, pH=8.5, 8 wt% PEG 8,000 in a 1 : 1 ratio (all from Sigma Aldrich).

D1D2, the sub-complex from the human snRNP spliceosome core particle (PDB entry 1B34 [85]), crystallized over 72 hrs at room temperature by preparing a crystallization batch with final concentrations of 6 mg/ml D1D2, 62 mM sodium citrate pH 5.2, 125 mM ammonium acetate, 9 vol% glycerol, 26 wt/vol PEG 4,000 (all Sigma Aldrich). D1D2 was purified as previously reported [85].

All globular proteins, concanavelin, glucose isomerase and trypsin, crystalized

readily in vapor diffusion, micro batch, and our emulsion system. The heterodimer D1D2 formed crystals in vapor phase and our emulsion system only. In microbatch a thick protein skin grew at the droplet interphase potentially depleting all the protein from the drop. We thus conclude that the PFPE-PEG-PFPE surfactant system is well suited to emulsify crystallization trials. Future work should investigate compatibility of the surfactant with other proteins. In particular in membrane protein crystallization, detergents are part of the crystallization cocktail, which might interact with the PFPE-PEG-PFPE surfactant.

5.4 X-ray transparent chip fabrication

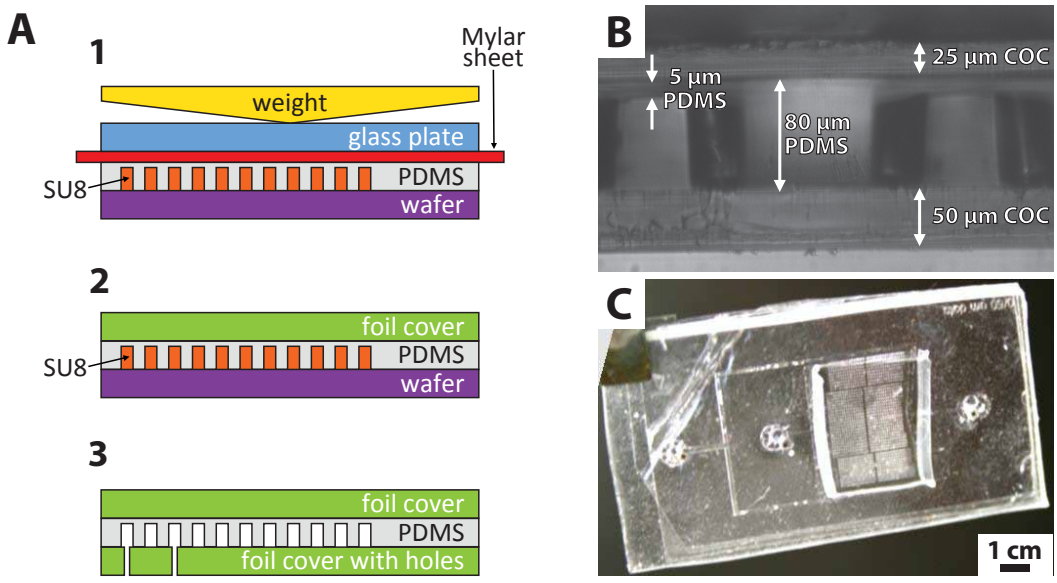

Figure 5.3: (A) We squeezed PDMS resin into a thin layer onto the SU8-master (1). After curing, we bonded a foil cover onto the featured PDMS (2) using a silane coupling-chemistry [86]. We then peeled the reinforced PDMS film and lidded the chip using another foil cover. (B) Cross-section and (C) top-view of a device made from COC-foil and PDMS.

Chips were fabricated by lidding featured PDMS with COC- or Kapton-foil (Figure 5.3). PDMS (Sylgard 184 from Dow Corning) with ratio 1 : 5 of curing agent

to base was molded on a standard SU8-master [37] by squeezing the uncured PDMS resin into a thin film using a glass plate and a weight. To facilitate release of the PDMS film we surface treated the master with a fluorophilic coating by spin-coating 1 : 20 Cytop CTL-809M in CTsolv.100E (both Bellex International) onto the master. We then baked the wafer for 1 hr at 150 ℃. We placed a 30 μm thin Mylar foil (DuPont) between PDMS and glass to allow for easy removal of the glass slide after PDMS curing. We pre-cured the PDMS for 4 hr at room temperature before we removed the weight and transfered the complete stack into the oven to drive the curing reaction to completion at 72 ℃ for another hour. We either used COC (TOPAS 5013 from Advanced Polymers) or Kapton (American Durafilm) depending on experimental requirements. COC is more brittle then Kapton, but has a lower water vapor permeability. The thinnest commercial COC we used was 25 μm thin TOPAS, while Kapton as thin as 8 μm can be purchased as bulk foil. We chemically bonded either substrate to the featured PDMS using a silane coupling chemistry [86]. In brief, both foil and PDMS are activated in an oxygen plasma and then incubated for 25 minutes in an aqueous solution of 1 vol% of a different silane each. The two silanes are such that they can form an epoxy bond when brought in contact. Upon removing foil and PDMS from the batch, we dried both with a stream of nitrogen gas and then carefully brought them in contact using tweezers to prevent trapping air bubbles between both layers. The chip was then incubated in the oven at 72 ℃ for 1 hr to maximize chemical cross-linking. The process was then repeated again to lid the other side of the chip. Upon assembly the chip was surface treated with a fluorophilic coating. For this, 1 : 20 Cytop CTX-109AE in CTsolv.100E (both Bellex International) was dead-end filled into the chip. The chip was then incubated at 90 ℃ for at least 12 hrs to evaporate the solvent away and also to accelerate chemical cross-linking between fluoropolymer and chip surface.

5.5 *In-situ* diffraction

We mounted the x-ray transparent chip into a custom acrylic frame to collect diffraction data (Figure 5.4). The acrylic frame was cut to shape from 3 mm thick acrylic sheet using a 40 W CO_2 Hobby Laser cutter with a 1.5" focus lens (Full Spectrum Laser). To port into the foil-chip we drilled through holes into the acrylic frame with the laser cutter. Blunt needle pins (23 gauge) were then placed into the through holes and glued into position with 5 minute Epoxy. We connected #30 AWG PTFE tubing (Cole Palmer) to the pins using PDMS cubes with through holes punched into them using 0.75 mm Harrison Uni-Core biopsy punches (Ted Pella). Buna O-rings with 70 durometer, size 002 (McMaster Carr) were then used to seal foil-chip to the hollow metal pins. For easy alignment the o-rings were fit into a 1 mm thick PET spacer that also was fabricated with the laser cutter. X-ray transparent foil-chips where mounted into a frame for the duration of each experiment. Each frame was held together by 10 self taping 3/16" Pan Head 2-28 Phillips screws (McMaster Carr) to lock the chip into position and to minimize flow induced inside the chip from mechanically bending the thin foil chip. To mount the frame-chip assembly in the synchrotron we machined a stainless steel adapter that a frame could be mounted onto using two screws (Figure 5.4 B).

As a proof of principle experiment we fabricated a x-ray transparent dropspot chip [87] that can hold up to 8000 emulsion droplets in cavities with 150 μm diameter each (Figure 5.3 B&C). These cavities arrest droplets into position and prevent them from creaming to one side of the chip. We then produced a monodisperse $\sim$90 μm diameter emulsion of 30 mg/ml glucose isomerase, 100 mM Ammonium Sulfate, pH 7.3, 20 wt% PEG 10000 final concentration in a standard dropmaker (Figure 5.1 B). Droplets exiting the dropmaker were immediately routed into the x-ray transparent dropspot

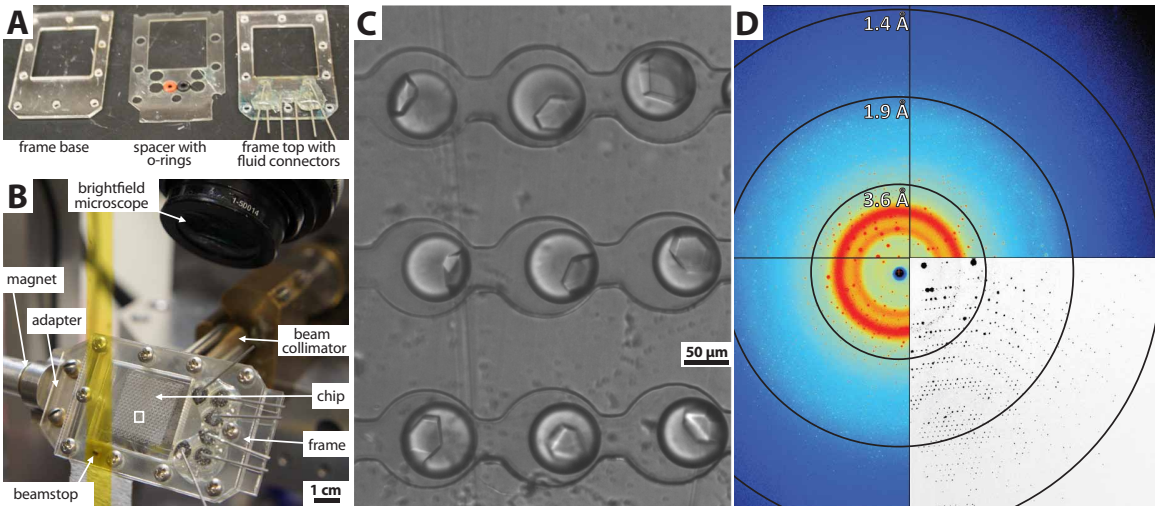

Figure 5.4: (A) We used a laser-cut frame to hold and to port into the X-ray transparent chip. (B) X-ray transparent chip inside the Cornell MacChess F1 beamline. (C) Glucose isomerase crystals inside of the microfluidic device. Using a motorized stage, each crystal can be centered in the collimated X-ray beam. The beam is 100 μm in diameter. (D) Representative diffraction pattern of a glucose isomerase crystal taken at room temperature from inside the chip. Crystals diffracted down to 1.37 resolution with a mosaicity as low as 0.04. The bottom right quadrant shows the diffraction pattern after background subtraction.

chip by simply plumbing the dropmaker outlet into the dropspot inlet. After the dropspot chip was loaded we dead-end plugged its outlet, except for one inlet where we kept HFE7500 oil entering the chip using hydrostatic pressure to compensate for oil evaporation from the chip. We incubated the chip at room temperature for three days and monitored crystallization. Crystals grew to about 50 by 40 by 30 μm in size at room temperatrue ($\sim$25℃). We then collected x-ray diffraction data at the Cornell MacChess F1 beamline. For each crystal we took ten consecutive one degree rotation diffraction patterns with 5 s exposures for each frame. We collected diffraction patterns for a total of 151 crystals from three dropspot chips.

5.6 X-ray structure determination by molecular replacement

Diffraction spots were indexed with HKL-2000 (HKL Research), we selected 230 frames from 72 crystals out of the full set of 151 glucose isomerase crystals using following criteria: from the preliminary analysis of integrating 10 frames per crystal, we observed mosaicities mostly below 0.1. Therefore we excluded frames with higher mosaicity from the set. In addition, frames with chi-squared x and y values above 1 were rejected. The remaining 230 frames represented 80 % of the Ewald sphere, suggesting that the crystals were randomly oriented inside the emulsion drops and that we were able to obtain the required angles for a full diffraction set to scale the intensities.

All 230 frames were then merged into a scale-file using Scalepack from HKL research. This scale-file was then used to solve the structure by molecular replacement using the Phenix software package. Refinements steps were done by simulated annealing and group B factors along with manual refinement (Table 5.2). As the in-put

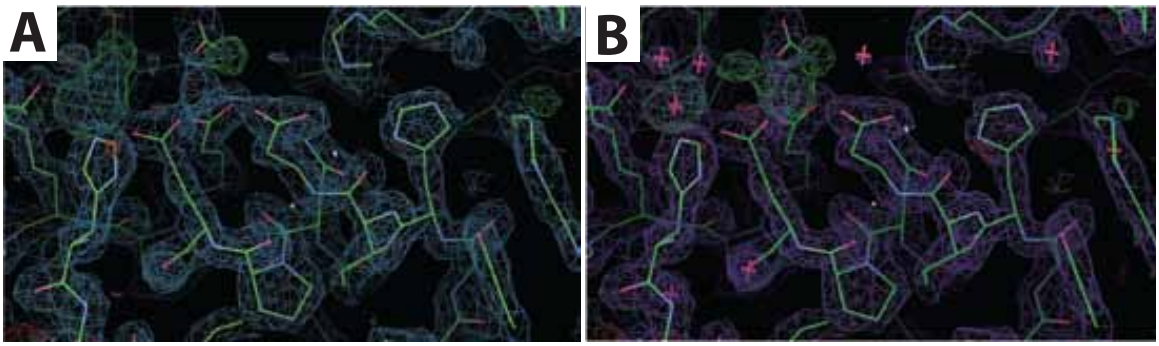

Figure 5.5: Electron density with structure model (A) before and (B) after refinement. Red crosses in (B) mark excluded electron density. Green polygons mark extra electron density that was present in the data, but not accounted for in the model, while red polygons mark election density that was expected due to the model, but absent in the data.

Table 5.2: Model statistics during different cycles of refinement in Phenix via simulated annealing and group B factors along with manual refinement.

	Refinement 1 Simulated annealing without water	**Refinement 2** Update water	**Refinement 3** Group B factors
R-work start	0.2083	0.2020	0.1799
R-free start	0.237	0.2403	0.2113
R-work final	0.2012	0.1803	0.1579
R-free final	0.2455	0.2116	0.1959
Ramachandran % favored	96.36	97.14	97.14
Ramachandran % outliers	0.26	0.26	0.26
Start RMS (bonds)	0.008	0.012	0.008
Final RMS (bonds)	0.008	0.008	0.008
Start RMS (angles)	1.082	1.224	1.068
Final RMS (angles)	1.088	1.068	1.078
Figure Of Merit (FOM)	0.4	0.5	0.86
Isotropic mean B	13.23		

model for phasing, we used the previously published glucose isomerase structure 8XIA from *Streptomyces rubiginosus* with 95 % identity from the protein data bank [77] (Table 5.3 and Figure 5.5).

Table 5.3: Final x-ray structure results after model building by molecular replacement in Phenix.

	8XIA from [77]	**this work**
Space Group	I222	I222
a (Å)	93.9	93.94
b (Å)	99.7	99.46
c (Å)	102.9	102.84
unique Observations	35493	30600
resolution Å	1.9	2.0
(completeness in resolution range)	(91)	(92.6)
total No. Atoms	3357	3047
(No. H_2O)	(306)	(295)
R	0.131	0.1579

5.7 Conclusion

We could grow monodisperse crystals packaged in emulsion droplets, with one crystal per drop. Crystals grew in identical conditions and could be batch processed. We built a X-ray transparent chip to collect diffraction patterns from these crystals at room temperature at high throughput. We could solve the structure of glucose isomerase by molecular replacement down to 2.0 Å resolution by merging room temperature datasets from 72 crystals of about 50 by 40 by 30 μm in size. Our chip is easy to fabricate and simple to operate without the need of controlling valves. In ongoing efforts, we seek to fabricate thinner chips so that diffraction data can be collected from crystals smaller then 10 μm. For this we are exploring new materials like Silicon Nitrite [88]. Future work will focus on automating crystal injection into the beam, to enable high throughput serial X-ray crystallography [89, 90] in standard synchrotron radiation.

5.8 Acknowledgements

We thank Kelsey Anthony for helping with the D1D2 and glucose isomerase purification and D1D2 crystallization trials, Frank Mello from the Brandeis Machine Shop for fabricating the stainless steel magnet adapter, and Daniel Pommeranz Krummel, Sol Gruner, Jeney Wierman, Marian Szebenyi, Irina Kriksunov, David Schuller, Chae Un Kim, Mike Cook, and Scott Smith for help and discussions with the protein X-ray crystallography. This work was supported by the NSF MRSEC (DMR-0820492) and NSF MWN 1209518. CHESS is supported by the NSF & NIH/NIGMS via NSF award DMR-0936384, and the MacCHESS resource is supported by NIH/NIGMS award GM103485.

Chapter 6

En Route to Signal Inversion in Chemical Computing

Michael Heymann, Kyle I. Harrington, Jordan Pollack, Seth Fraden

(An excerpt of this chapter was originally published in the Proceedings of the Alife XII Conference, Odense, Denmark, 2010[91]. Reproduced with permission from the Royal Society of Chemistry.)

6.1 Abstract

We investigated the Belousov-Zhabotinzky (BZ) reaction as a substrate for computation. Expanding on previous research we present a new technique that utilizes two modes of the BZ reaction, excitation and oscillation, and selective diffusive coupling. We show in simulation that this technique can be used to invert input signals, providing the logical operator, NOT. Our system can readily compute NOR, which when connected in multiples is sufficient for simulating any other logical operator. Furthermore, progress to experimentally implement these operators and to wire them into

circuits using soft lithography and replica molding is presented.

6.2 Introduction

To synthesize living systems the field of artificial life has explored numerous substrates, physical and virtual. Chemical substrates have been gaining in popularity with recent advances in chemical computation [92, 93] and cognition [94]. In Braitenbergs series of vehicles of increasing cognitive complexity a key turning point is the introduction of inhibitory threshold devices, allowing for the use of numbers, logic, and basic memory [95]. Though to an extent the latter two properties have been introduced in our choice substrate, the Belousov-Zhabotinzky (BZ) reaction, true inhibition in the BZ has not been achieved. Here we applied the novel concept of inhibitory coupling [96] to design signal inverting logic gates. Using BZ substrate, various logic gates have been implemented experimentally or by computer simulation. Gorecki has simulated the gates AND and OR, as well as the MAJORITY function. Adamatzky showed XOR and AND in a related experimental substrate. Collision dynamics of BZ waves have also been exploited to annihilate signals [97]. To our knowledge, binary negation-based gates such as the computationally universal gates NAND and NOR [98] have not been implemented. We simulated the computation of NOT and NOR in a heterogeneous BZ substrate and synthesized a NOT gate prototype.

6.3 Results

We designed negation-based gates using a light-sensitive implementation of the BZ reaction [99]. Our system is composed of two elements: excitatory and oscillatory

domains connected through a filter. Both domains are chemically identical, but differ in the amount of projected light. The illumination was tuned such that induction of a small perturbation (input) into the excitatory domain can ignite a full excitation. The oscillatory domain follows an unsuppressed periodic trajectory. Using oil as a chemical filter allows for signal inversion. The filter is selective and only non-polar species such as bromine (Br_2) can permeate across [96]. Thus, a wave traveling from the excitable towards the oscillatory domain will temporarily increase the Br_2 in the oscillatory domain. Br_2 is then readily converted back to the inhibitor Br^-, which will delay the oscillation in the oscillatory domain (Figure 6.1).

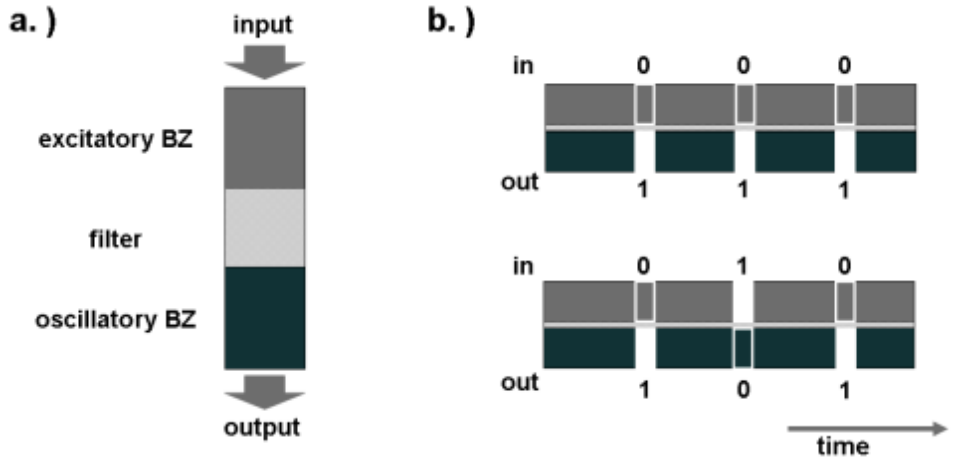

Figure 6.1: Inverter circuit and idealized space-time plots for signal inversion. The excitatory domain is conducting input waves into the oscillatory patch (a). Without input, the oscillatory domain transitions between oxidized (white, logic state true) and reduced (dark, logic state false) state (b, top). Due to the inhibitory coupling incoming waves will suppress and delay oscillations in the oscillatory domain into a later reading frame (b, bottom).

We verify our concept by simulating a simplified reaction-diffusion system of the light-sensitive BZ reaction [99]. We integrate chemical turnover numerically in each BZ domain and compute the flux between compartments. Assuming fast diffusion within compartments, we reduce their size to a single point. Though a single inverter

is sufficient for an inhibitory connection, we extend upon simple signal inversion to realize a NOR gate by combining two inverters. Prototypes were constructed by casting BZ catalyst immobilized on silica gel into patterned PDMS slabs (Figure 6.2). Hydrophobic PDMS walls were designed to separate BZ domains and act as selective chemical filters. Preliminary experimentation suggests our substrate can couple BZ domains within circuits (Figure 6.3).

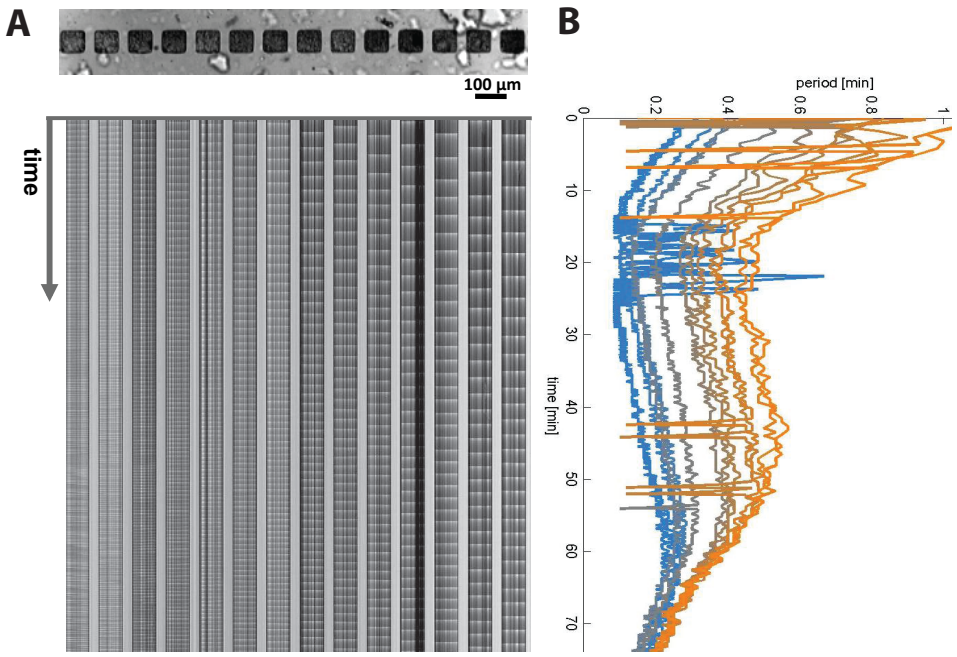

Figure 6.2: (A) 1D patch arrangement of BZ catalyst gels in PDMS (top) and space-timeplot of gel patch oscillations (bottom). We pattern thin PDMS films on microscope slides using standard soft-lithograph. BZ silica gel is then cast into the features and covered with BZ substrate. (B) Periods of the gel patches in (A). We observed high frequency oscillations with periods on the order of 4s.

6.4 Conclusion

The BZ reaction offers a wide range of interesting dynamics. We have described a technique capable of inverting input signals, and presented supporting simulations

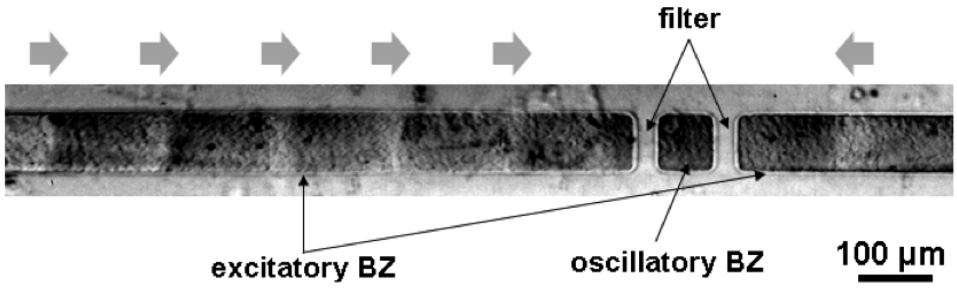

Figure 6.3: NOR gate prototype. Catalyst immobilized on silica gel was cast into patterned PDMS slabs. Hydrophobic PDMS walls separate BZ domains and act as chemical filters. Action potential like input waves (indicated by grey arrows) propagate towards and couple into the central oscillatory domain.

along with preliminary experimental results. This work suggests that the BZ reaction may be a useful substrate for the synthesis of minimally cognitive agents. Future work will utilize finite element analysis to quantitatively identify parameters for optimal input timing and delay strength. Experimental efforts will focus on increasing the robustness of single logic operators as well as connecting them into functional circuits to achieve universal computation at the microscopic scale in a chemical substrate.

Acknowledgements

We thank Andrew Adamatzky, Milos Dolic, Irving Epstein, Marcin Leda, Ning Li, and Hector Ochoa Gonzales for helpful discussions.

Bibliography

[1] McPherson, A. (1999) *Crystallization of Biological Macromolecules*. (Cold Spring Harbor Laboratory Press).

[2] Gasser, U, Weeks, E. R, Schofield, A, Pusey, P. N, & Weitz, D. A. (2001) *Science* **292**, 258–62.

[3] Haxton, T. K & Whitelam, S. (2013) *Soft Matter* **9**, 6851–61.

[4] Bloustine, J, Virmani, T, Thurston, G, & Fraden, S. (2006) *Physical Review Letters* **96**, 087803.

[5] Annunziata, O, Paduano, L, Pearlstein, A. J, Miller, D. G, & Albright, J. G. (2006) *The Journal of Physical Chemistry B* **110**, 1405–15.

[6] Selimović, S, Jia, Y, & Fraden, S. (2009) *Crystal Growth & Design* **9**, 1806–10.

[7] Li, L & Ismagilov, R. F. (2010) *Annual Review of Biophysics* **39**, 139–58.

[8] Leng, J & Salmon, J.-B. (2009) *Lab on a Chip* **9**, 24–34.

[9] Shim, J.-U, Cristobal, G, Link, D. R, Thorsen, T, & Fraden, S. (2007) *Crystal Growth & Design* **7**, 2192–4.

[10] Hansen, C. L, Skordalakes, E, Berger, J. M, & Quake, S. R. (2002) *Proceedings of the National Academy of Sciences of the United States of America* **99**, 16531–6.

[11] Hansen, C & Quake, S. R. (2003) *Current Opinion in Structural Biology* **13**, 538–44.

[12] Hansen, C. L, Classen, S, Berger, J. M, & Quake, S. R. (2006) *Journal of the American Chemical Society* **128**, 3142–3.

[13] Anderson, M. J, Hansen, C. L, & Quake, S. R. (2006) *Proceedings of the National Academy of Sciences of the United States of America* **103**, 16746–51.

[14] Zheng, B, Roach, L. S, & Ismagilov, R. F. (2003) *Journal of the American Chemical Society* **125**, 11170–1.

[15] Zheng, B, Tice, J. D, Roach, L. S, & Ismagilov, R. F. (2004) *Angewandte Chemie (International Ed. in English)* **43**, 2508–11.

[16] Zheng, B, Gerdts, C. J, & Ismagilov, R. F. (2005) *Current Opinion in Structural Biology* **14**, 548–55.

[17] Gerdts, C. J, Elliott, M, Lovell, S, Mixon, M. B, Napuli, A. J, Staker, B. L, Nollert, P, & Stewart, L. (2008) *Acta Crystallographica Section D, Biological Crystallography* **64**, 1116–22.

[18] Gerdts, C. J, Stahl, G. L, Napuli, A, Staker, B, Abendroth, J, Edwards, T. E, Myler, P, Van Voorhis, W, Nollert, P, & Stewart, L. J. (2010) *Journal of Applied Crystallography* **43**, 1078–83.

[19] Li, L, Du, W, & Ismagilov, R. (2010) *Journal of the American Chemical Society* **132**, 106–11.

[20] Gerdts, C. J, Tereshko, V, Yadav, M. K, Dementieva, I, Collart, F, Joachimiak, A, Stevens, R. C, Kuhn, P, Kossiakoff, A, & Ismagilov, R. F. (2006) *Angewandte Chemie (International Ed. in English)* **45**, 8156–60.

[21] Selimović, S, Gobeaux, F, & Fraden, S. (2010) *Lab on a Chip* **10**, 1696–9.

[22] Talreja, S, Perry, S. L, Guha, S, Bhamidi, V, Zukoski, C. F, & Kenis, P. J. A. (2010) *The Journal of Physical Chemistry B* **114**, 4432–41.

[23] Stroock, A. D, Dertinger, S. K. W, Ajdari, A, Mezic, I, Stone, H. A, & Whitesides, G. M. (2002) *Science* **295**, 647–51.

[24] Malloggi, F, Pannacci, N, Attia, R, Monti, F, Mary, P, Willaime, H, Tabeling, P, Cabane, B, & Poncet, P. (2010) *Langmuir* **26**.

[25] Wang, P, Robert, L, Pelletier, J, Dang, W. L, Taddei, F, Wright, A, & Jun, S. (2010) *Current biology* **20**, 1099–103.

[26] Tien, J, Nelson, C. M, & Chen, C. S. (2002) *Proceedings of the National Academy of Sciences of the United States of America* **99**, 1758–62.

[27] Chemnitz, S, Tangen, U, Wagler, P, Maeke, T, & McCaskill, J. (2008) *Chemical Engineering Journal* **135**, S276–9.

[28] Stanford-Microfluidics-Foundry. (2013) *http://www.stanford.edu/group/foundry/multi height molds.html*.

[29] Mata, A, Fleischman, A. J, & Roy, S. (2006) *Journal of Micromechanics and Microengineering* **16**, 276–84.

[30] Farrens, S & Sood, S. (2012) *www.suss.com/fileadmin/user_upload/technical_publications/WP_WLP_PrecisionWafertoWaferPackaging_0801.pdf.*

[31] Stuart, C, Xu, Q, Tseng, R. J, Yang, Y, Hahn, H. T, Chen, Y, Wu, W, & Williams, R. S. (2006) *Journal of Vacuum Science & Technology B: Microelectronics and Nanometer Structures* **24**, 539–42.

[32] Rasband, W. (2013) *Available from: http://imagej.nih.gov/ij.*

[33] Sollier, E, Murray, C, Maoddi, P, & Di Carlo, D. (2011) *Lab on a Chip* **11**, 3752–65.

[34] Mikkelsen, M. B, Letailleur, A. A, Søndergård, E, Barthel, E, Teisseire, J, Marie, R, & Kristensen, A. (2012) *Lab on a Chip* **12**, 262–7.

[35] Bhattacharyya, A & Klapperich, C. M. (2007) *Biomedical Microdevices* **9**, 245–51.

[36] Romanowsky, M. B, Heymann, M, Abate, A. R, Krummel, A. T, Fraden, S, & Weitz, D. A. (2010) *Lab on a Chip* **10**, 1521–4.

[37] McDonald, J. C, Duffy, D. C, Anderson, J. R, Chiu, D. T, Wu, H, Schueller, O. J. A, & Whitesides, G. M. (2000) *Electrophoresis* **21**, 27–40.

[38] Zanzotto, A, Szita, N, Boccazzi, P, Lessard, P, Sinskey, A. J, & Jensen, K. F. (2004) *Biotechnology and Bioengineering* **87**, 243–54.

[39] Unger, M. A, Chou, H, Thorsen, T, Scherer, A, & Quake, S. R. (2000) *Science* **288**, 113–6.

[40] Abate, A. R, Romanowsky, M. B, Agresti, J. J, & Weitz, D. A. (2009) *Applied Physics Letters* **94**, 023503.

[41] Nisisako, T & Torii, T. (2008) *Lab on a Chip* **8**, 287–93.

[42] Rhee, M & Burns, M. A. (2009) *Lab on a Chip* **9**, 3131–43.

[43] Okushima, S, Nisisako, T, Torii, T, & Higuchi, T. (2004) *Langmuir* **20**, 9905–8.

[44] Chen, C.-H, Shah, R. K, Abate, A. R, & Weitz, D. A. (2009) *Langmuir* **25**, 4320–3.

[45] Zhou, J, Ellis, A. V, & Voelcker, N. H. (2010) *Electrophoresis* **31**, 2–16.

[46] Wang, Y, Lai, H.-H, Bachman, M, Sims, C. E, Li, G. P, & Allbritton, N. L. (2005) *Analytical Chemistry* **77**, 7539–46.

[47] Seo, M, Paquet, C, Nie, Z, Xu, S, & Kumacheva, E. (2007) *Soft Matter* **3**, 986–92.

[48] Abate, A. R, Krummel, A. T, Lee, D, Marquez, M, Holtze, C, & Weitz, D. A. (2008) *Lab on a Chip* **8**, 2157–60.

[49] Anderson, J. R, Chiu, D. T, Jackman, R. J, Cherniavskaya, O, McDonald, J. C, Wu, H, Whitesides, S. H, & Whitesides, G. M. (2000) *Analytical Chemistry* **72**, 3158–64.

[50] Dendukuri, D, Pregibon, D. C, Collins, J, Hatton, T. A, & Doyle, P. S. (2006) *Nature Materials* **5**, 365–9.

[51] Dendukuri, D, Panda, P, Haghgooie, R, Kim, J. M, Hatton, T. A, & Doyle, P. S. (2008) *Macromolecules* **41**.

[52] Bartolo, D, Degre, G, Nghe, P, & Studer, V. (2008) *Lab on a Chip* **8**, 274–9.

[53] Abate, A. R, Poitzsch, A, Hwang, Y, Lee, J, Czerwinska, J, & Weitz, D. A. (2009) *Physical Review E* **80**, 026310.

[54] Salmon, J.-B & Leng, J. (2009) *Comptes Rendus Chimie* **12**, 258–69.

[55] Shim, J.-u, Patil, S. N, Hodgkinson, J. T, Bowden, S. D, Spring, D. R, Welch, M, Huck, W. T. S, Hollfelder, F, & Abell, C. (2011) *Lab on a Chip* **11**, 1132–7.

[56] Song, S, Singh, A. K, Shepodd, T. J, & Kirby, B. J. (2004) *Analytical Chemistry* **76**, 2367–73.

[57] Chueh, B.-h, Huh, D, & Kyrtsos, C. (2007) *Analytical Chemistry* **79**, 3504–8.

[58] Kim, C, Ryu, C, Kim, B. W, Sim, S. J, Chae, H, Yoon, H. C, & Yang, S. S. (2007) *Journal of the Korean Physical Society* **51**, 993–9.

[59] Ou, J, Glawdel, T, Samy, R, Wang, S, Liu, Z, Ren, C. L, & Pawliszyn, J. (2008) *Analytical Chemistry* **80**, 7401–7.

[60] Scrimgeour, J, Cho, J. K, Breedveld, V, & Curtis, J. (2011) *Soft Matter* **7**, 4762–7.

[61] Anderson, M. J. (2009) Ph.D. thesis (California Institute of Technology).

[62] Boukellal, H, Selimovic, S, Jia, J, Cristobal, G, & Fraden, S. (2009) *Lab on a Chip* **9**, 331–8.

[63] Dertinger, S. K. W, Chiu, D. T, Jeon, N. L, & Whitesides, G. M. (2001) *Analytical Chemistry* **73**, 1240–6.

[64] Kissick, D, Wanapun, D, & Simpson, G. (2011) *Annual Review of Analytical Chemistry* **4**, 419–37.

[65] Haupert, L. M & Simpson, G. J. (2011) *Methods* **55**, 379–86.

[66] Wampler, R. D, Kissick, D. J, Dehen, C. J, Gualtieri, E. J, Grey, J. L, Wang, H.-F, Thompson, D. H, Cheng, J.-X, & Simpson, G. J. (2008) *Journal of the American Chemical Society* **130**, 14076–7.

[67] Mertz, J & Moreaux, L. (2011) *Optics Communications* **196**, 325–30.

[68] Padayatti, P, Palczewska, G, & Sun, W. (2012) *Biochemistry* **51**, 1625–37.

[69] Selimović, S, Kim, W. Y, Kim, S. B, Jang, Y. H, Lee, W. G, Khabiry, M, Bae, H, Jambovane, S, Hong, J. W, & Khademhosseini, A. (2011) *Analytical Chemistry* **83**, 2020–8.

[70] Chayen, N. E. (2004) *Current Opinion in Structural Biology* **14**, 577–83.

[71] Bergfors, T. (2003) *Journal of Structural Biology* **142**, 66–76.

[72] Chayen, N. E, Saridakis, E, & Sear, R. P. (2006) *Proceedings of the National Academy of Sciences of the United States of America* **103**, 597–601.

[73] Li, L, Mustafi, D, Fu, Q, Tereshko, V, Chen, D. L, Tice, J. D, & Ismagilov, R. F. (2006) *Proceedings of the National Academy of Sciences of the United States of America* **103**, 19243–8.

[74] Dhouib, K, Khan Malek, C, Pfleging, W, Gauthier-Manuel, B, Duffait, R, Thuillier, G, Ferrigno, R, Jacquamet, L, Ohana, J, Ferrer, J.-L, Théobald-Dietrich, A, Giegé, R, Lorber, B, & Sauter, C. (2009) *Lab on a Chip* **9**, 1412–21.

[75] Guha, S, Perry, S. L, Pawate, A. S, & Kenis, P. J. A. (2012) *Sensors and Actuators B* **174**, 1–9.

[76] Dombrowski, R. D, Litster, J. D, Wagner, N. J, & He, Y. (2010) *AIChE Journal* **56**, 79–91.

[77] Carrel, H. L, Glusker, J. P, Burger, V, Manfret, F, Tritsch, D, & Bielmann, J.-F. (1989) *Proceedings of the National Academy of Sciences of the United States of America* **86**.

[78] Akella, S. (2014) Ph.D. thesis (Brandeis University).

[79] Holtze, C, Rowat, A. C, Agresti, J. J, Hutchison, J. B, Angilè, F. E, Schmitz, C. H. J, Köster, S, Duan, H, Humphry, K. J, Scanga, R. A, Johnson, J. S, Pisignano, D, & Weitz, D. A. (2008) *Lab on a Chip* **8**, 1632–9.

[80] ProtParam-tool. (2013) *http://web.expasy.org/protparam*.

[81] Wetter, L. R & Deutsch, H. F. (1951) *Journal of Biological Chemistry* **192**, 237–42.

[82] Walsh, K. A. (1970) *Methods in Enzymology* **19**, 41–63.

[83] Entlicher, G, , Koštíř, J, & Kocourek, J. (1971) *Biochimica et Biophysica Acta* **236**, 795–7.

[84] Vuolanto, A, Uotila, S, Leisola, M, & Visuri, K. (2003) *Journal of Crystal Growth* **257**, 404–11.

[85] Kambach, C, Walke, S, Young, R, Avis, J. M, de la Fortelle, E, Raker, V. A, Lührmann, R, Li, J, & Nagai, K. (1999) *Cell* **96**, 375–87.

[86] Tang, L & Lee, N. (2010) *Lab on a Chip* **10**, 1274–80.

[87] Schmitz, C. H. J, Rowat, A. C, Köster, S, & Weitz, D. A. (2009) *Lab on a Chip* **9**, 44–9.

[88] Weinhausen, B & Köster, S. (2013) *Lab on a Chip* **13**, 212–5.

[89] Chapman, H. N, Fromme, P, Barty, A, White, T. A, Kirian, R. A, Aquila, A, Hunter, M. S, Schulz, J, DePonte, D. P, Weierstall, U, Doak, R. B, Maia, F. R. N. C, Martin, A. V, Schlichting, I, Lomb, L, Coppola, N, Shoeman, R. L, Epp, S. W, Hartmann, R, Rolles, D, Rudenko, A, Foucar, L, Kimmel, N, Weidenspointner, G, Holl, P, Liang, M, Barthelmess, M, Caleman, C, Boutet, S, Bogan, M. J, Krzywinski, J, Bostedt, C, Bajt, S, Gumprecht, L, Rudek, B, Erk, B, Schmidt, C, Hömke, A, Reich, C, Pietschner, D, Strüder, L, Hauser, G, Gorke, H, Ullrich, J, Herrmann, S, Schaller, G, Schopper, F, Soltau, H, Kühnel, K.-U, Messerschmidt, M, Bozek, J. D, Hau-Riege, S. P, Frank, M, Hampton, C. Y, Sierra, R. G, Starodub, D, Williams, G. J, Hajdu, J, Timneanu, N, Seibert, M. M, Andreasson, J, Rocker, A, Jönsson, O, Svenda, M, Stern, S, Nass, K, Andritschke, R, Schröter, C.-D, Krasniqi, F, Bott, M, Schmidt, K. E, Wang, X, Grotjohann, I, Holton, J. M, Barends, T. R. M, Neutze, R, Marchesini, S, Fromme, R, Schorb, S, Rupp, D, Adolph, M, Gorkhover, T, Andersson, I, Hirsemann, H, Potdevin, G, Graafsma, H, Nilsson, B, & Spence, J. C. H. (2011) *Nature* **470**, 73–7.

[90] Boutet, S, Lomb, L, Williams, G, & Barends, T. (2012) *Science* **337**, 362–4.

[91] Heymann, M, Harrington, K. I, Pollack, J, & Fraden, S. (2010) *Proceedings of Artificial Life XII.* pp. 166–7.

[92] Adamatzky, A. (2009) *Encyclopedia of Complexity and Systems Science* pp. 7548–65.

[93] Gorecki, J, Gorecka, J, & Igarashi, Y. (2009) *Natural Computing* **8**, 473–92.

[94] Dale, K & Husbands, P. (2010) *Artificial Life* **16**, 1–19.

[95] Braitenberg, V. (1986) *Vehicles - Experiments in Synthetic Psychology.* (MIT Press).

[96] Toiya, M, Vanag, V, & Epstein, I. (2008) *Angewandte Chemie (International Ed. in English)* **120**, 7867–9.

[97] de Lacy Costello, B, Toth, R, Stone, C, Adamatzky, A, & Bull, L. (2009) *Physical Review E* **79**, 26114.

[98] Sheffer, H. (1913) *Transactions of the American Mathematical Society* **14**, 481–488.

[99] Vanag, V. K & Epstein, I. R. (2009) *The Journal of Chemical Physics* **131**, 104512.